

# Submesoscale processes and Mixing

March 2, 2021

J. Gula<sup>1,2</sup> J. Taylor<sup>3</sup>, A. Shcherbina<sup>4</sup>, & A. Mahadevan<sup>5</sup>

<b>0.1</b>	<b>Introduction</b>	2
<b>0.2</b>	<b>Life-cycle of submesoscale fronts</b>	9
0.2.1	Frontogenesis	9
0.2.2	Instability of surface boundary layer fronts	11
0.2.3	Submesoscale processes at the bottom of the ocean	24
0.2.4	The influence of vertical mixing on the evolution of a submesoscale front	32
0.2.5	Frontal arrest and routes to dissipation	36
<b>0.3</b>	<b>Redistribution of density and restratification at the submesoscale</b>	37
0.3.1	Restratification induced by submesoscale processes	37
0.3.2	Competition between destratification and restratification of a front	39
0.3.3	Bottom boundary layer mixing and restratification	41
<b>0.4</b>	<b>Redistribution of passive tracers and particles</b>	42
0.4.1	Conservative tracers	43
0.4.2	Mixing and transport of reactive tracers	44
0.4.3	Impacts on the dispersion of buoyant material	45
0.4.4	Dispersion by the deep submesoscale currents	45
<b>0.5</b>	<b>Conclusion and future directions</b>	46

- 
1. Univ Brest, CNRS, IRD, Ifremer, Laboratoire d'Océanographie Physique et Spatiale (LOPS), IUEM, Brest, France
  2. Institut Universitaire de France (IUF)
  3. Department of Applied Mathematics and Theoretical Physics, University of Cambridge, Cambridge CB3 0WA, UK
  4. Applied Physics Laboratory, University of Washington, Seattle, Washington
  5. Woods Hole Oceanographic Institution, Woods Hole, Massachusetts

## ABSTRACT

In this chapter, we discuss the links between oceanic submesoscale (100 m–10 km) processes and mixing. Submesoscale currents occur on lateral scales of 100 m–10 km in the ocean and are associated with density fronts and filaments, vortices and topographic wakes at the surface and in the ocean’s interior. In most cases, submesoscale processes do not directly contribute to mixing, however they have an important role in cascading energy and tracer variance from the largely adiabatic mesoscale down to the scales at which diapycnal mixing can occur. Submesoscale currents re-distribute water properties, including buoyancy, momentum, heat, freshwater, and biogeochemical tracers. While submesoscale instabilities enhance vertical exchange, they drive an efficient restratification of the upper ocean. They can also have a strong impact in the bottom boundary layer where they generate turbulent mixing and export mixed waters out of the bottom boundary layer.

We first present an overview of submesoscale dynamics, starting with frontogenesis and several important instability mechanisms that generate submesoscale currents in the ocean: mixed-layer baroclinic, gravitational, symmetric and inertial/centrifugal instabilities. Particular attention is paid to the complex role of turbulent mixing in the formation, evolution and decay of submesoscale features. We then discuss the impact of the different types of submesoscale processes on the redistribution of density and passive tracers, including impacts for some biogeochemical tracers and buoyant material.

### KEYWORDS

Submesoscale currents, Frontogenesis, Mixed-layer instability, Symmetric instability, Centrifugal/Inertial instability, Restratiification, Tracer dispersion, Vertical fluxes

## 0.1 INTRODUCTION

Submesoscale currents in the ocean take form of intense jets and vortices with horizontal scales of 100 m – 10 km and time scales of hours to weeks (Thomas et al., 2008; McWilliams, 2016). Almost invariably they are associated with the

- 5 corresponding hydrographic features – fronts, filaments, and spirals of matching scales. This association is so tight that dynamic and hydrographic terms are commonly used interchangeably in the literature (e.g., “jets” and “fronts”). High resolution satellite observations of Sea Surface Temperature (SST) and ocean color or high resolution numerical models (Fig. 1) are exposing the ubiquity of
- 10 such submesoscale frontal features at the surface.

The upper end of the submesoscale is historically defined by the scales of the mesoscale eddies, which vary as the local Rossby deformation radius  $R_d$ , from roughly 10 km at high-latitudes to 200 km near to the equator (Chelton et al., 1998; LaCasce and Groeskamp, 2020). The lower end of the submesoscale is typically taken as the scales corresponding to the turbulent boundary layer depth  $h_{bl} = 10 \text{ m} – 100 \text{ m}$ , below which the flow becomes more isotropic. Thus,

submesoscale currents occupy intermediate space and time scales between quasi-geostrophic mesoscale eddies and the fully three-dimensional turbulence.

Dynamically, submesoscale processes are characterized by order one Rossby and Froude numbers (Thomas et al., 2008). The Rossby number, arising from the relative scaling of the inertial and Coriolis terms in the equations of motion, is defined as  $Ro = U/fL$ , where  $U$  is the characteristic horizontal velocity scale,  $f$  is the local Coriolis frequency and  $L$  is the characteristic horizontal length scale. The Froude number, characterizing the balance of inertia and stratification effects, is defined as  $Fr = U/NH$ , where  $N = \sqrt{\partial b/\partial z}$  is the buoyancy frequency,  $b = -g\rho/\rho_0$  is the buoyancy,  $\rho$  is the density,  $\rho_0$  is a constant reference density, and  $H$  is the characteristic vertical scale. The order one Rossby and Froude numbers imply that stratification, rotation, and inertia are all important to submesoscale dynamics.

The important role played by submesoscale currents has been realized over the last decade (McWilliams, 2016). Submesoscales can transfer energy from larger quasi-balanced motions to small-scale three-dimensional turbulence, thereby providing a route to dissipation (Müller et al., 2005). Submesoscale currents re-distribute water properties, including momentum, buoyancy, heat, freshwater, and biogeochemical tracers (Poje et al., 2014; Shcherbina et al., 2015; Mahadevan, 2016). The strong heterogeneities they generate at the ocean surface have important implications for modulating air-sea fluxes of energy and in structuring marine ecosystems (Lévy et al., 2018) and bacterioplankton communities (Fadeev et al., 2020). The strong vertical velocities they generate drive significant irreversible vertical fluxes of mass, buoyancy, and materials that control stratification of the upper ocean as well as exchanges between the surface layer and the ocean interior (Balwada et al., 2018; Su et al., 2018; Uchida et al., 2019; Mahadevan et al., 2020; Bachman and Klocker, 2020).

Submesoscale currents are generated and influenced by a number of different processes, which are summarized in Fig. 2 and will be discussed in detail in the following section. The stirring induced by mesoscale eddies can generate density fronts and filaments (Hoskins and Bretherton, 1972; McWilliams, 1984). This can be described using quasi-geostrophic theories where it corresponds to a direct cascade of tracer variance toward smaller scales (see review in Lapeyre (2017) and Chapter 9 for a more detailed description). The fronts and filaments can then further intensify due to self-sustained frontogenesis (Hoskins and Bretherton, 1972). Ageostrophic effects are more important to ‘submesoscale frontogenesis’ when submesoscale currents deform fronts (Shakespeare and Taylor, 2013; Barkan et al., 2019).

Another efficient mechanism to generate submesoscale currents is mixed-layer baroclinic instability (MLI) (Haine and Marshall, 1999; Boccaletti et al., 2007; Fox-Kemper et al., 2008). MLI is an extension of the classical geostrophic baroclinic instability, but with a smaller horizontal scale due to the reduced Rossby deformation radius in the mixed layer. However, since the corresponding Rossby number is typically  $O(1)$ , ageostrophic effects are more pronounced in

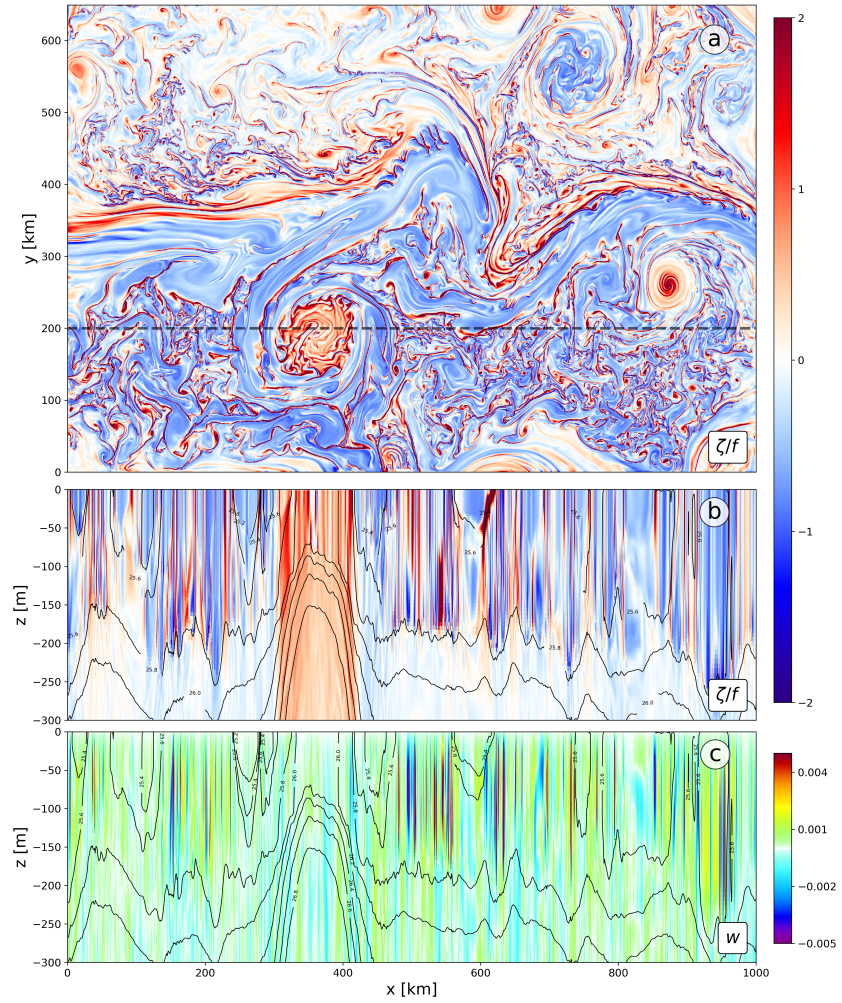


**FIGURE 1** (a) Vertical vorticity  $\zeta$  normalized by  $f$  at the surface in the wintertime Gulf Stream in a submesoscale-resolving ( $\delta = 500$  m) simulation. (b) Vertical section of vertical vorticity along the dashed line in panel (a), and (c) Vertical section of vertical velocity.

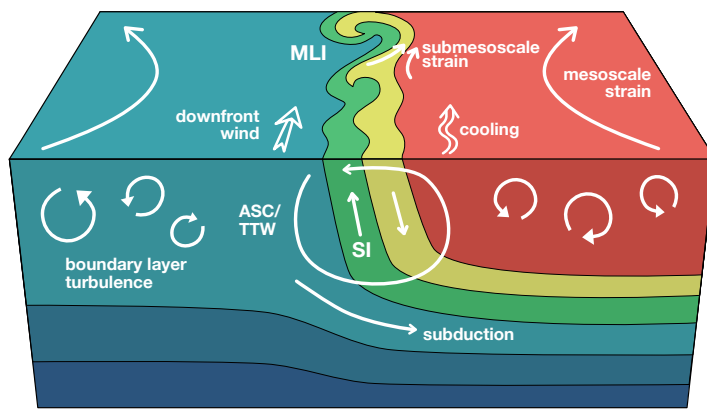


**FIGURE 2** Idealized depiction of various submesoscale processes discussed in this chapter. Convergent mesoscale strain drives frontogenesis. Surface cooling or a down-front wind can make the front unstable to symmetric instability (SI). The frontogenetic strain and vertical mixing drive an ageostrophic secondary circulation (ASC), which, in the latter case, can be described as a turbulent thermal wind (TTW) balance. Submesoscale eddies develop through mixed layer instability (MLI) which drives further frontogenesis and localizes boundary layer turbulence and subduction of water into the thermocline.

MLI compared to the mesoscale baroclinic instability. Submesoscale currents can also be generated by inherently ageostrophic “symmetric” instabilities triggered by atmospheric forcing at fronts (Taylor and Ferrari, 2009; Thomas and Taylor, 2010; D’Asaro et al., 2011). The ageostrophic nature of submesoscale dynamics explains a number of profound characteristics of submesoscale features including intense upwelling/downwelling, rapid re-stratification, and production of small-scale turbulence.

In most cases submesoscale currents do not directly contribute to mixing in the form of tracer homogenization, which occurs near sub-millimeter Batchelor scales due to molecular diffusion. However, submesoscale dynamics have an important role in cascading energy and tracer variance from the largely adiabatic mesoscale down to scales where three-dimensional turbulence can take over (McWilliams et al., 2001). Submesoscale instabilities can facilitate a dynamical route to molecular diffusion by extracting energy from the geostrophically balanced flow and triggering secondary turbulent flows leading to small-scale turbulent mixing (Molemaker et al., 2010; D’Asaro et al., 2011; Brüggemann and Eden, 2015). Furthermore, submesoscale processes are typically associated with enhanced vertical velocities (Mahadevan and Tandon, 2006; Klein and Lapeyre, 2009) and vertical fluxes of heat, buoyancy and tracers in the mixed layer (Mahadevan et al., 2012; Su et al., 2018). They can thus induce complex profiles of vertical stratification that influence vertical mixing in the surface layer and maintain elevated mixing efficiency at submesoscale fronts.

Submesoscale processes play a particularly important role in modulating the upper ocean stratification. Even though stratification changes are primarily driven by air-sea exchanges and vertical mixing, lateral stirring becomes increasingly important near density fronts (Rudnick and Ferrari, 1999; Ferrari and Rudnick, 2000). Submesoscale processes alter the horizontal and vertical density gradients in a number of interrelated and competing ways: Frontogenesis sharpens horizontal gradients of density and may also alter the vertical stratification if frontogenetic strain is depth-dependent. At the same time, submesoscale ageostrophic secondary circulation associated with frontogenesis, MLI and symmetric instability (SI) tends to decrease isopycnal slope in the upper ocean, partially transforming horizontal density gradients into vertical – a process commonly described as submesoscale frontal slumping and restratification.

Submesoscale dynamics have been originally studied in the open ocean surface boundary layer, although they are also prevalent in coastal or estuarine environments. The local Rossby deformation radius on the continental shelf can be on the order of 1-10 km or smaller, such that structures at this scale may be classified as mesoscale in the literature. However, the Rossby and Froude numbers nearshore can reach and exceed  $O(1)$  values typical of open ocean submesoscale regimes (*e.g.*, Capet et al., 2008a; Dauhajre et al., 2017; Wang et al., 2021). Thus, littoral dynamics share many processes with open ocean submesoscale dynamics, albeit modified by the strong influence of topographic, wave-driven, tidal, and freshwater runoff effects.

105 Energetic submesoscale currents can also be found at the bottom of the deep ocean in the presence of steep topography as on continental slopes, seamounts and ridges. An illustration showing submesoscale currents in a numerical model at 1500 m depth around the Mid-atlantic ridge is shown in Fig. 3. High resolution numerical models have highlighted efficient mechanisms for topographic generation of submesoscale currents through interactions of geostrophic flows with steep topographic slopes (Molemaker et al., 2015; Gula et al., 2015b), ridges (Vic et al., 2018), and seamounts (Srinivasan et al., 2019). These interactions can lead to elevated local kinetic energy dissipation (Gula et al., 2016) and diapycnal mixing (Dewar et al., 2015) through triggering of centrifugal instability or intense horizontal shear instability and to the formation of submesoscale coherent vortices. Observations have recently confirmed that bottom currents interacting with sloping topography can trigger submesoscale instabilities with important implications for mixing and upwelling of deep-ocean waters (Ruan et al., 2017; Naveira Garabato et al., 2019). Theoretical and process studies are beginning 110 to highlight the full extent of the role played by submesoscale processes in the bottom boundary layer (Wenegrat et al., 2018a; Wenegrat and Thomas, 2020). Furthermore, submesoscale baroclinic instability of the bottom boundary layer might be instrumental in driving restratification in the deep ocean and exporting mixed water from the bottom boundary layer (Callies, 2018; Wenegrat et al., 115 2018a). These results are particularly timely because of the recent realization that the energetic mixing near ocean boundaries plays a fundamental role in driving the global ocean circulation, as detailed in Chapters 3 and 7 of this book. The role played by bottom submesoscale processes in this picture is still largely unknown.

120 130 Field observations of submesoscale phenomena are complicated by their small horizontal scales, rapid evolution, and spatial heterogeneity. Much of our understanding of submesoscale dynamics has been obtained from numerical modelling (Fig. 1), either through dedicated process studies (*e.g.*, Boccaletti et al., 2007) or realistic high-resolution simulations (*e.g.*, Capet et al., 2008b). Observational verification of this understanding, however, remains a challenge. While satellite SST or ocean color routinely reveal an abundance of submesoscale 135 structures at the surface, they cannot be used to reconstruct the underlying velocity fields. Furthermore, the footprints of the current generation of satellite altimeters ( $\approx 100$  km) is unable to resolve submesoscale currents. Satellite measurements from the Surface Water and Ocean Topography mission (SWOT, Fu and Ferrari, 2008) will soon provide a global coverage of Sea Surface Height (SSH) at better resolution (15-30 km, Morrow et al. 2019). However, reconstructing the surface velocity from SSH at these scales remains a challenging task due to the presence of internal waves and other unbalanced motions with 140 similar spatial scales (Torres et al., 2018). Promising results have been obtained for the observation of intense submesoscale fronts with airborne optical and radar measurements of their surface roughness signature (Raschle et al., 2017, 145 2020), but they are limited to a small number of examples so far.

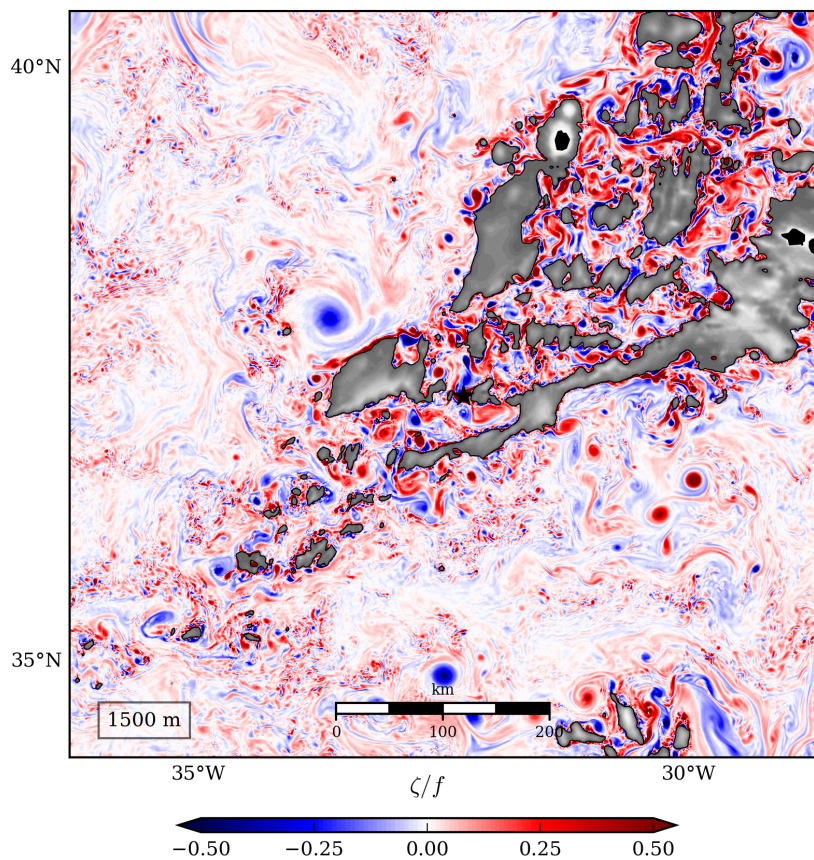


**FIGURE 3** Instantaneous relative vorticity  $\zeta = v_x - u_y$  at 1500 m depth over the Mid-Atlantic Ridge. Data from a numerical simulation with  $\delta x = 750$  m horizontal resolution. Image adapted from Vic et al. (2018).

Only a few dedicated observational programs have been able to acquire data with enough spatial and temporal resolution to allow a quantitative characterisation of submesoscale currents in the surface layer, *e.g.*, AESOP (D’Asaro et al., 2011; Johnson et al., 2020a), LATMIX (Shcherbina et al., 2013), OSMOSIS (Buckingham et al., 2016), ASIRI (Wijesekera et al., 2016), CARTHE-LASER (D’Asaro et al., 2020), and CALYPSO (Mahadevan et al., 2020). Such programs usually require a combination of mooring arrays, multiple ships, autonomous underwater vehicles, or swarms of surface drifters to allow for a computation of submesoscale gradients of velocity and tracers. Observations of submesoscale currents at the bottom of the ocean are even more difficult to obtain and the examples are still rare (Naveira Garabato et al., 2019).

In the following section, we review the important mechanisms driving the formation, evolution, and decay of submesoscale fronts. These include frontogenesis in section 0.2.1 and the instabilities that develop on submesoscale fronts in section 0.2.2. Aspects specific to the bottom boundary are developed in section 0.2.3. The evolution of fronts in the presence of turbulent mixing is discussed in section 0.2.4, and finally the decay of submesoscale fronts is discussed in section 0.2.5. In section 0.3, we discuss the impact of the different types of submesoscale processes on the redistribution of density, focusing in particular on the effects on the restratification of the surface layer, but also on the mixing and restratification induced by submesoscale processes in the bottom boundary layer. In section 0.4, the impact on the redistribution of passive tracers is discussed, including impacts for some biogeochemical tracers and buoyant material. Finally we present our conclusions and perspectives in section 0.5.

## 0.2 LIFE-CYCLE OF SUBMESOSCALE FRONTS

### 0.2.1 Frontogenesis

Open ocean fronts develop and intensify through a process known as frontogenesis. The mathematical theory of frontogenesis, which describes the intensification of cross-front density gradients in response to an imposed background flow, was originally developed in the atmospheric context (Hoskins and Bretherton, 1972; Hoskins, 1982) and later applied to the upper ocean (Macvean and Woods, 1980; Lapeyre and Klein, 2006; Capet et al., 2008c). An extensive review of oceanic frontogenesis has recently been published by McWilliams (2021), we briefly recall the important aspects of frontogenesis below.

A classical description of frontogenesis involves the sharpening of favorably aligned lateral density gradients by a straining flow, disruption of geostrophic balance for the along-front flow, and generation of an ageostrophic secondary circulation (ASC), see Fig. 2. This secondary circulation acts to restore geostrophic balance by advectively restratifying the flow, *i.e.*, tilting the isopycnals toward the horizontal by bringing warm/light water over the top of cold/dense water. The ASC thus forms an overturning cell in the cross-front/vertical plane, with

- 190 upwelling ( $w' > 0$ ) on the light side ( $\rho' < 0$  or  $b' > 0$ ) and downwelling ( $w' < 0$ ) on the dense side ( $\rho' > 0$  or  $b' < 0$ ), where  $w$  is the vertical velocity and primes denote deviations from a cross front average. The associated vertical buoyancy flux is thus always positive, i.e.  $w'b' > 0$ , corresponding to restratification of the front.

195 A canonical setup to study frontogenesis considers a density front embedded in a large-scale horizontal flow with a uniform strain rate:  $u_d = -\alpha x$ ,  $v_d = \alpha y$ , as illustrated in Fig. 4a. This configuration is well suited for mesoscale strain-induced frontogenesis, which is one of the fundamental factors leading to submesoscale currents. For quasi-geostrophic flow, strain-induced frontogenesis 200 causes the cross-front gradient to increase at an exponential rate (e.g.,  $\partial_x C \sim \exp \alpha t$  for a tracer  $C$ ) (Washington, 1964).

205 On the dense side of a finite-width front, the ASC is convergent at the ocean surface (see Fig. 4). This amplifies the convergence associated with the large-scale strain flow and accelerates frontogenesis. Using the inviscid semi-geostrophic equations, Hoskins and Bretherton (1972) showed that this leads to super-exponential intensification of the density gradient and the collapse of the front into a singularity in finite time. A similar result was found in the generalized theory of Shakespeare and Taylor (2013) which included gravity waves and other ageostrophic effects. The asymptotic model derived by Barkan et al. (2019) even 210 shows that when  $Ro \sim 1$  the sharpening rate is primarily determined by the near-surface convergent motions associated with the ASC, rather than the large-scale strain flow. A bulk estimate for the vertical buoyancy fluxes of a front undergoing submesoscale frontogenesis is shown to be:  $w'b' \sim -Hl(t)\delta(t)\partial_x b(t)$ , with  $\delta(t) < 0$  the velocity divergence due to the ASC,  $l(t) \approx l(t_0)(1 + \delta(t_0)t)$  the 215 width of the front at a time  $t > t_0$ . Therefore, any pre-existing density front, for example generated by the stirring of mesoscale eddies, may rapidly form an intense submesoscale front with order one  $Ro$  and further sharpen at a super-exponential rate.

220 A variant of frontogenesis applicable to dense filaments – sometimes called filamentogenesis – has been proposed by McWilliams et al. (2009). A dense filament corresponds to a surface density maximum formed by two parallel fronts with opposite-sign density gradient, as shown in Fig. 4b. The deformation flow acting on a favorably aligned dense filament causes an even more rapid narrowing and stronger surface convergence and downwelling at its center than 225 for an isolated front of similar scale and  $Ro$ . Instantaneous values of the vertical velocity at the center of dense filaments can reach  $\sim 1 \text{ cm s}^{-1}$  in realistic submesoscale-resolving simulations (Gula et al., 2014).

230 In general, any ASC in a finite-width front will necessarily have a zone of surface convergence, and therefore may contribute additional frontogenetic feedback. An example of this will be discussed in section 0.2.4 dealing with the ASC induced by vertical mixing.

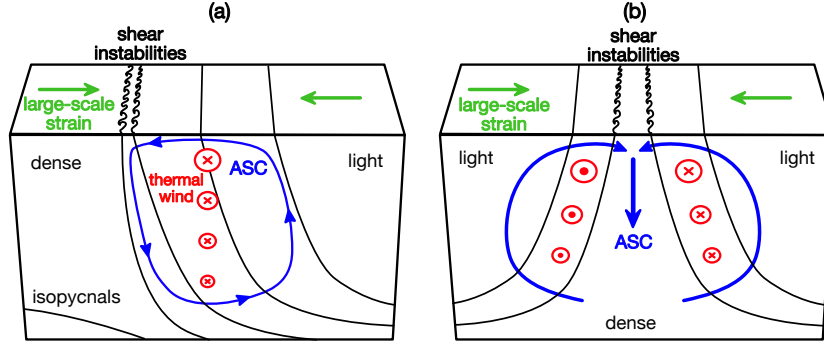


**FIGURE 4** Sketches of surface-layer frontogenesis caused by a large-scale deformation flow for (a) a front and (b) a dense filament, adapted from McWilliams (2016).

### 0.2.2 Instability of surface boundary layer fronts

Once fronts form and intensify through the process of frontogenesis, they can become susceptible to a variety of instabilities which generate additional submesoscale currents. These instabilities include: mixed-layer instability (MLI); symmetric instability (SI); ageostrophic anticyclonic instability (McWilliams et al., 2004); and horizontal shear instability (Munk et al., 2000).

In this section, we briefly describe the theory for the two most studied submesoscale instabilities: MLI and SI. Although the focus in this section will largely be on processes in the upper ocean, similar physical mechanisms are also active in the bottom boundary layer, as will be discussed in section 0.2.3.

#### 0.2.2.1 Mixed-layer baroclinic instability

Mixed-layer instability (MLI) is an upper-ocean equivalent of the classical interior baroclinic instability (Haine and Marshall, 1999), as illustrated in Fig. 5. It is one of the most important sources of submesoscale currents in the surface mixed-layer, and it has been extensively studied over the last decade using theory, idealised numerical simulations (Boccaletti et al., 2007; Fox-Kemper et al., 2008; Callies et al., 2016), and realistic submesoscale resolving numerical simulations (Capet et al., 2008c).

Baroclinic instabilities in the ocean interior are the primary source for the generation of mesoscale eddies at horizontal scales around or larger than the Rossby deformation radius:

$$R_{int} = \frac{N_{int} H_{tot}}{f}, \quad (1)$$

where  $N_{int}$  is the stratification in the ocean interior and  $H_{tot}$  the ocean depth. MLI is a similar mechanism taking place in the weakly stratified surface layer,

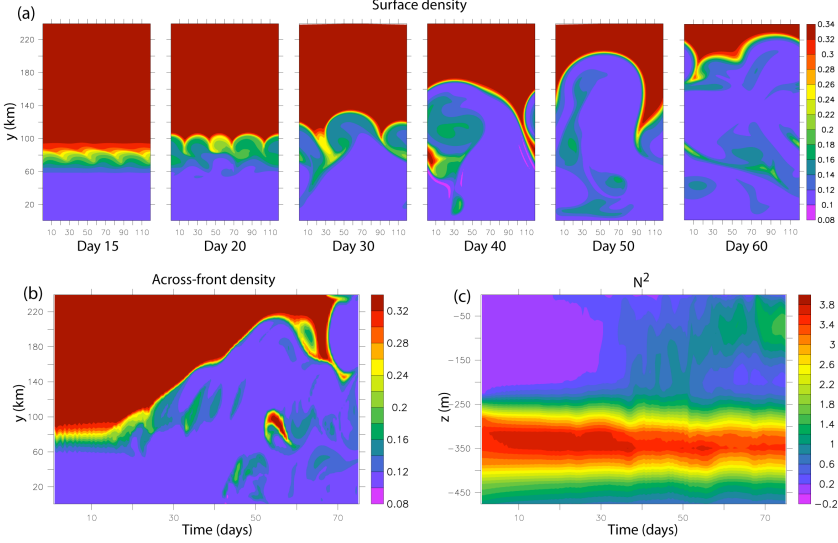


**FIGURE 5** (a) Time sequence of the surface density anomaly showing the evolution of MLI in an idealized simulation of a front. (b) Evolution of the across front density and (c) of the vertical stratification. Adapted from Mahadevan et al. (2010).

which has its own deformation radius,

$$R = \frac{NH}{f} \quad (2)$$

where  $N$  and  $H$  are now the stratification and thickness of the weakly stratified surface layer.  $R$  is typically much smaller than  $R_{int}$  because of the relative smallness of the mixed layer stratification  $N$  and thickness  $H$ . Typical values of  $N = 10^{-3} \text{ s}^{-1}$ ,  $H = 100 \text{ m}$  and  $f = 10^{-4} \text{ s}^{-1}$  lead to  $R = 1 \text{ km}$ , which is well within the submesoscale range.

Submesoscale MLI can be analyzed to leading order using the Eady model (Eady, 1949). Although the ageostrophic secondary circulation can be large during submesoscale frontogenesis (Barkan et al., 2019), most theoretical studies of submesoscale instability have considered a balanced basic state. The basic state in the Eady model consists of a fluid with constant horizontal and vertical buoyancy gradients bounded from above and below by flat, rigid surfaces. The basic state velocity has a constant vertical shear in thermal wind balance with the horizontal buoyancy gradient. Specifically, if the basic state buoyancy is

$$b = N^2 z - M^2 y, \quad (3)$$

then the basic state geostrophic velocity is

$$u = \frac{M^2}{f} z, \quad (4)$$

where in this case  $z$  can be defined with respect to an arbitrary reference level of no motion.

As discussed in Eady (1949) and Stone (1966), there is one non-dimensional parameter in the system describing the evolution of linear, inviscid perturbations to this basic state. This parameter can be formulated as a ‘balanced Richardson number’,

$$Ri \equiv \frac{N^2}{u_z^2} = \frac{N^2 f^2}{M^4}, \quad (5)$$

where  $u_z$  is the thermal wind shear. Note that  $Ri$  is equivalent to the gradient Richardson number formed with the thermal wind shear. If we use the thermal wind to define a characteristic velocity scale,  $U = M^2 H/f$ , where  $H$  is the vertical distance between the top and bottom boundaries, and set a characteristic horizontal length scale based on the isopycnal slope, i.e.  $L = N^2 H/M^2$ , then we can relate the Rossby number to the balanced Richardson number,

$$Ro \equiv \frac{U}{fL} = \frac{M^4}{f^2 N^2} = \frac{1}{Ri}. \quad (6)$$

The analysis in Eady (1949) assumed that  $Ri \gg 1$  and hence  $Ro \ll 1$ , while Stone (1966) generalized this to arbitrary  $Ri$  and  $Ro$ . When  $Ri \gg 1$ , the most unstable mode in the Eady model is independent of the cross-front direction (the  $y$ -direction in the basic state given above) and corresponds to the classical baroclinic instability. In this context, MLI can be viewed as baroclinic instability in the limit when  $Ri, Ro \sim 1$ , both characteristic of submesoscales in the mixed layer.

The wavelength of the most unstable perturbation for baroclinic instability is  $L \approx 4R$ , assuming that  $Ri \gg 1$  as in Eady (1949). Taking into account ageostrophic effects, the wavelength of the fastest-growing MLI mode becomes  $L_{MLI} \approx 4\sqrt{1 + Ri^{-1}}R$  (Stone, 1966; Nakamura, 1988), such that the instability is shifted to larger scales at small  $Ri$  if  $R$  is fixed. This scaling, with a typical value  $Ri = 0.8$ , has been used to estimate the surface MLI wavelength on a global scale by Dong et al. (2020b). The mixed-layer depth and stratification have been computed either directly from Argo profiles or from 1D simulations of the Generalized Ocean Turbulence Model (GOTM) embedded in the outputs of a global MITgcm simulation at submesoscale-permitting resolution (LLC4320, see Su et al. (2018)), as shown in Fig. 3 and 4 of Chapter 4. The results obtained for  $L_{MLI}$  with GOTM and a KPP parameterization for vertical mixing are reproduced in Fig. 6a. The zonal median MLI wavelength varies from about 30 km in the tropics to 1 km at high-latitudes. Given that the grid-spacing of a model needs to be at least  $L_{MLI}/8$  to properly resolve the eddies generated due to MLI, the requirements are still pretty high for models to be able to resolve MLI on a global scale.

MLI draws its energy from the available potential energy associated with horizontal buoyancy gradients – and converts it to kinetic energy. The energy

310 source term in the equation of evolution for the perturbation kinetic energy is the  
 buoyancy flux,  $w'b'$ , where perturbations to the background flow are denoted  
 $(\cdot)'$  (Capet et al., 2008c). The buoyancy flux associated with MLI is thus  
 always positive and restratifies the mixed layer by distorting and tilting isopycnal  
 surfaces (Fig. 5). Re-stratification by MLI represents a leading-order process in  
 the mixed-layer buoyancy budget, as discussed in Sec. 0.3.

315 The conversion of available potential energy to kinetic energy happens near  
 the instability scale. From there we may expect two possible non-linear energy  
 cascades: an inverse energy cascade towards larger scales – typical of geostrophic  
 turbulence (see review in Klein et al., 2019) –, and a forward energy cascade  
 320 driven by ageostrophic motions and loss of balance (Capet et al., 2008d). MLI  
 transfers energy preferentially to larger scales (Boccaletti et al., 2007; Fox-  
 Kemper et al., 2008), as visible in Fig. 5. Interactions between submesoscale  
 325 eddies generated by MLI lead to an inverse cascade of energy, from the scale  
 corresponding to the local wavelength of the fastest growing mode of MLI  
 towards the mesoscale. This process helps to energize mesoscale eddies (Qiu  
 et al., 2014; Sasaki et al., 2014; Schubert et al., 2020) and may explain the  
 330 interannual to decadal variations of the mesoscale kinetic energy (Sasaki et al.,  
 2020). However, the submesoscale eddy field generated as a result of MLI  
 also develops sharp frontal features with active frontogenesis, which can lead to  
 secondary instabilities and small-scale turbulence, and feed the forward cascade  
 335 of energy (Schubert et al., 2020), as discussed in Sec. 0.2.5.

340 The available potential energy density at a front scales as  $H^2|\nabla_h b|$ . The  
 depth of the mixed-layer is thus a critical parameter controlling the energy  
 of submesoscale eddies generated by MLI. This explains why submesoscale  
 345 flows are expected to be stronger in winter, when the mixed-layer deepens due  
 to the strong negative buoyancy forcing, than in summer. This seasonality is  
 confirmed by both the numerical simulations (Mensa et al., 2013; Sasaki et al.,  
 2014; Brannigan et al., 2015; Ajayi et al., 2021) and in-situ observations (Callies  
 et al., 2015). In winter, the energized submesoscale flows produce surface kinetic  
 350 energy spectra that scale like  $k^{-2}$  at scales below 100 km, with  $k$  the horizontal  
 wavenumber, which is typical of active submesoscale regimes. In summer,  
 the spectra are steeper and scale like  $k^{-3}$ , which is typical of interior quasi-  
 geostrophic turbulence. More precisely, a global analysis using outputs from  
 the submesoscale-permitting LLC4320 simulation has highlighted two phases  
 355 in this seasonal transition (Khatri et al., 2020). In late autumn the spectra first  
 flatten as  $k^{-2}$  at scales  $< 50$  km, but still follow a  $k^{-3}$  slope at larger scales  
 (100-300 km). In late winter, the spectra flattens as  $k^{-2}$  also at large scales  
 due to the inverse energy cascade initiated by MLI energizing the mesoscales.  
 There is also a time-lag – about one month in the Kuroshio region – between the  
 360 mixed-layer thickness maximum and the submesoscale energy peak due to the  
 competition between the production of eddy kinetic energy due to the vertical  
 buoyancy fluxes and the nonlinear energy cascade to larger scales (Dong et al.,  
 2020a). The surface MLI wavelength, which scales linearly with  $H$ , also has

355 a strong seasonality with a median value 1.6 times smaller in summer (10 km) than winter (16 km) globally (Fig. 6a).

360 Submesoscale baroclinic instability modes can sometimes extend below the mixed-layer for particular stratification profiles. This can happen in the presence of a weakly-stratified transition layer between the mixed layer and the thermocline, as observed by Zhang et al. (2020). The presence of a weakly-stratified sublayer and an equatorward buoyancy gradient can also lead to the onset of Charney baroclinic instability, leading to an intensification of near-surface frontal activity (Capet et al., 2016).

#### 0.2.2.2 Symmetric Instability

365 When ageostrophic perturbations are considered in the linear stability analysis of the Eady model described previously, an additional set of instabilities are permitted. This was shown by Stone (1966, 1970, 1972) in a series of papers on non-geostrophic instability in the Eady model.

370 When  $Ri < 1$ , an ageostrophic instability develops where the most unstable perturbations are independent of  $x$  (the cross-front direction)<sup>6</sup> Stone (1966) and Hoskins (1974) refer to this mode as ‘symmetric instability’ - a term that originated in studies of growing axisymmetric perturbations to a circular baroclinic vortex (Eliassen and Kleinschmidt, 1957; Ooyama, 1966).

375 In an unbounded, inviscid fluid, the most unstable mode of symmetric instability (hereafter SI) has motion that is aligned with isopycnals (Stone, 1966; Taylor and Ferrari, 2009). As a result, the buoyancy perturbations associated with SI modes are typically small. Whereas the baroclinic instabilities (including MLI) gain energy predominately from background potential energy, SI modes gain energy primarily at the expense of the thermal wind shear (Taylor and Ferrari, 2010).

380 Hoskins (1974) showed that the criterion for SI can be written  $f q < 0$  where  $q = (\omega + f \hat{\mathbf{k}}) \cdot \nabla b$  is the Ertel potential vorticity (PV) and  $f$  is the Coriolis parameter<sup>7</sup>. This immediately presents a paradox: Since PV is materially conserved in an adiabatic, inviscid fluid, no re-arrangement of fluid parcels within a region with  $f q < 0$  will change the bulk PV (Thorpe and Rotunno, 1989). 385 A resolution of this paradox was proposed by Taylor and Ferrari (2009) who showed that the along-isopycnal motions associated with SI become unstable to a secondary Kelvin-Helmholtz shear instability. The resulting small-scale turbulence quickly increases  $f q$  by exchanging PV with a neighboring stable region (*e.g.*, the pycnocline) or driving a stabilising PV flux through the ocean surface.

---

6. Note that Stone (1966) also refers to Kelvin-Helmholtz instabilities, but Vanneste (1993) showed that these do not develop in the Eady model.

7. Note that a more general criterion for SI can be introduced for curved fronts in cyclogeostrophic or gradient wind balance. The resulting expression becomes  $(1 + Cu) f q < 0$ , where  $Cu$  is a nondimensional number quantifying the curvature of the flow, as discussed in Buckingham et al. (2021a,b)

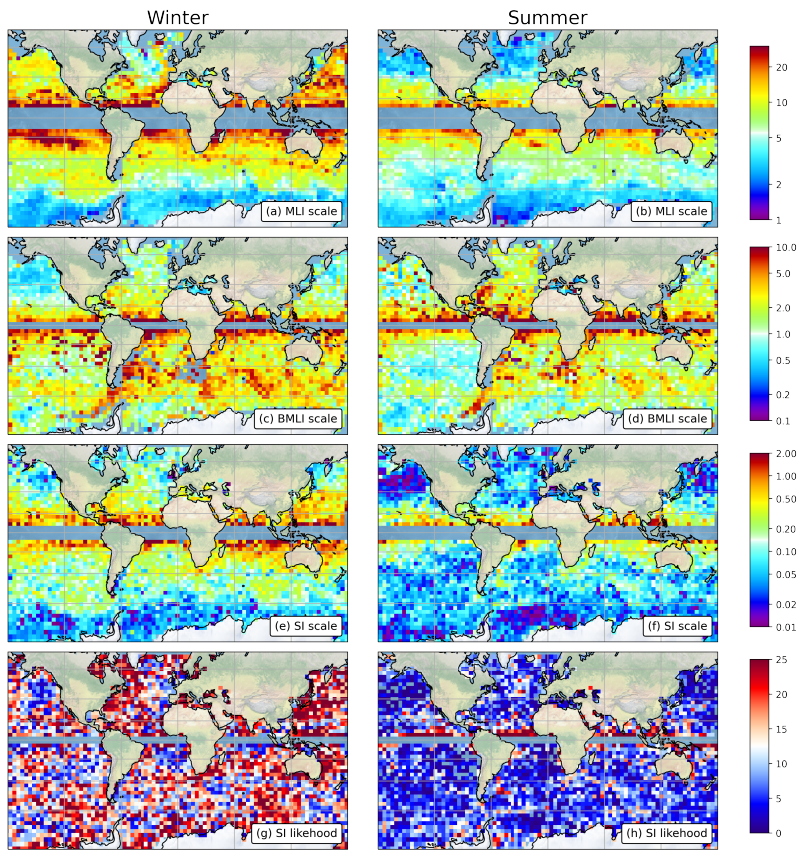


**FIGURE 6** Global distributions of the fastest-growing wavelength (in km) for (a,b) MLI, (c,d) BMLI, and (e-f) SI, and relative likelihood (%) of SI (g-h). Results in (left) winter (February in the Northern Hemisphere and August in the Southern Hemisphere) and (right) summer (August in the Northern Hemisphere and February in the Southern Hemisphere). Figure adapted from Dong et al. (2020b) and Dong et al. (2021).

SI can also be viewed as a hybrid of inertial and gravitational instability (Haine and Marshall, 1999). Due to the close connection with gravitational instability, SI is sometimes referred to as ‘slantwise convection’ (e.g. Straub and Kiladis, 2002; van Haren and Millot, 2009), although as discussed below it is important to note that the energetics of SI are distinct from convection. Inertial instability arises when the vertical component of the relative vorticity is anticyclonic and larger in magnitude than the Coriolis parameter, i.e.  $\zeta/f < -1$ . When the stratification is unstable ( $N^2 < 0$ ) gravitational (or Rayleigh-Taylor) instability can develop.

For inviscid motions that are independent of  $x$ , the absolute momentum,  $\mathcal{M} \equiv u - fy$ , is conserved,

$$\frac{D\mathcal{M}}{Dt} = 0, \quad (7)$$

where  $D/Dt$  is the material derivative. In this case, the Ertel PV can be written

$$q = \mathcal{M}_y b_z - \mathcal{M}_z b_y. \quad (8)$$

For simplicity, consider the Northern Hemisphere ( $f > 0$ ) where SI develops when  $q < 0$  or

$$\frac{\mathcal{M}_y}{\mathcal{M}_z} < \frac{b_y}{b_z}. \quad (9)$$

In other words, SI can occur when isopycnals are steeper than surfaces of constant absolute momentum.

Given the close relationship between gravitational, inertial, and symmetric instability, a natural question is how to identify the dominant instability from a given set of conditions (e.g., in observations or an ocean model). This is particularly relevant within strong fronts where all three instabilities can result in slantwise motion. The potential vorticity is not sufficient to distinguish between these instabilities since gravitational and inertial instability are also typically associated with  $f q < 0$  (with  $f N^2 < 0$  in the case of gravitational instability and  $f \zeta < 0$  in the case of inertial instability). One approach, which was utilized by Thomas et al. (2013) is to classify the dominant instability associated with a given basic state using the energetics of the most unstable mode.

In a barotropic fluid, gravitational instability converts background potential energy into kinetic energy through the vertical buoyancy flux ( $w' b' > 0$ ), while inertial instability grows via lateral shear production. As noted above, SI predominately extracts energy from the vertical shear associated with the thermal wind via geostrophic shear production (Taylor and Ferrari, 2010). By identifying the energy source associated with the most unstable perturbations, the dominant instability can be identified from a given basic state.

As was shown by Thomas et al. (2013), for a basic state that is in thermal wind balance, the dominant type of instability depends on the balanced Richardson number (5). Thomas et al. (2013) introduced what we call the ‘Thomas angle’,

Th, where

$$\text{Th} \equiv \tan^{-1} \left( -\frac{|\nabla_h b|^2}{f^2 N^2} \right). \quad (10)$$

The Thomas angle is analogous to the Turner angle (often denoted Tu) which is used to distinguish different types of double-diffusive instabilities.

430 The Thomas angle re-maps the possible values of  $Ri \in (-\infty, \infty)$  to  $-\pi \leq \text{Th} \leq 0$ . For a basic state consisting of uniform gradients in velocity and buoyancy, the flow is unstable when  $\text{Th} < \text{Th}_c$ , where

$$\text{Th}_c \equiv \tan^{-1} \left( -\frac{\zeta}{f} \right), \quad (11)$$

435 is the critical angle. Figure 7 shows regions of gravitational instability (GI), symmetric instability (SI), and inertial instability (II). When the basic state vertical vorticity is anticyclonic, inertial/symmetric instability (II/SI) occurs when  $-45^\circ < \text{Th} < \text{Th}_c$ . In this region the lateral shear production (LSP) is the dominant energy source for the growing perturbations, although the geostrophic shear production (GSP) also contributes. For a stably stratified barotropic fluid (440  $N^2 > 0$  and  $|\nabla b| = 0$ ), the Thomas angle is  $\text{Th} = 0$ , and instability is only possible if  $\text{Th}_c > 0$ , which corresponds to  $\zeta < -f$ , the usual criterion for inertial instability.

445 Although an unstable buoyancy profile ( $N^2 < 0$ ) corresponds to  $\text{Th} < -\pi/2$ , the buoyancy flux (BFLUX) is the dominant source of energy only for  $\text{Th} < -3\pi/4$ . When  $-3\pi/4 < \text{Th} < -\pi/4$  for anticyclonic vorticity and  $-3\pi/4 < \text{Th} < \text{Th}_c$  for cyclonic vorticity, the GSP is the dominant source of perturbation kinetic energy. Within these limits, Thomas et al. (2013) distinguish between SI/GI when  $N^2 < 0$  and SI when  $N^2 > 0$ . Although the linear stability analysis was performed for a simple basic state with uniform velocity and buoyancy gradients, Thomas et al. (2013) showed that the Thomas angle was able to identify various dynamical regimes when applied *pointwise* to large-eddy simulations of the Gulf Stream front.

### 0.2.2.3 Forced symmetric instability

455 Since the criterion for SI depends on the sign of the potential vorticity, and since PV is materially conserved, the development of SI is closely tied to boundary forcing that is capable of changing the bulk PV. Further, since the growth rate of SI is relatively fast (with a characteristic timescale  $\sim 1/f$ ), simulations and observations indicate that SI can quickly respond to de-stabilizing forcing and maintain  $f q \approx 0$  (e.g., Thomas and Taylor, 2010; Thomas et al., 2013, 2016). Following Taylor and Ferrari (2010), we use ‘forced symmetric instability’ (or forced SI) to refer to the nonlinear manifestation of symmetric instability that develops in response to de-stabilizing surface forcing.

460 Thomas (2005) discussed the conditions required for destruction of PV by surface forcing and showed that  $f q$  is reduced when the surface of the ocean is

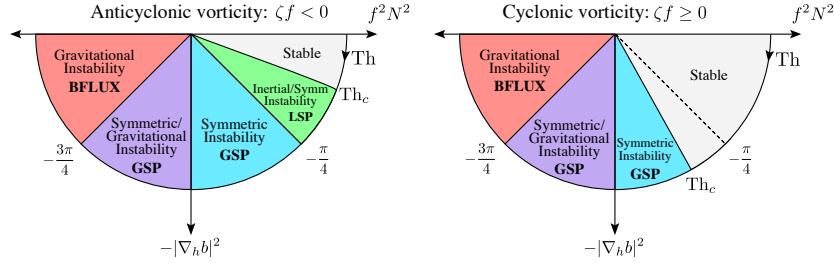


**FIGURE 7** Regimes of gravitational instability (GI), symmetric instability (SI) and inertial instability (II) as a function of the Thomas angle (Th) when the vertical component of the relative vorticity ( $\zeta$ ) is anticyclonic (left) and cyclonic (right). In each region, the dominant source of energy is labeled as follows: Buoyancy flux (BFLUX), Geostrophic shear production (GSP), and lateral shear production (LSP). Adapted from Thomas et al. (2013).

cooled by losing heat to the atmosphere, or when the surface wind stress points in the direction of the thermal wind - a so called ‘downfront wind’. In the case of a downfront wind, dense water tends to be drawn over light water by the cross-front Ekman flow acting on the horizontal density gradient associated with the front. When sampled at a fixed position, this cross-front advection will result in a decrease in the surface buoyancy. The rate of change in buoyancy induced by the cross-front Ekman flow can be quantified through the Ekman buoyancy flux (EBF):

$$\text{EBF} \equiv \mathbf{M}_E \cdot \nabla_h b, \quad (12)$$

where

$$\mathbf{M}_E = \tau_w \times \frac{f\hat{\mathbf{k}}}{\rho_0 f^2}, \quad (13)$$

is the Ekman transport,  $\tau_w$  is the wind stress,  $\nabla_h b$  is the horizontal buoyancy gradient,  $f$  is the Coriolis parameter, and  $\hat{\mathbf{k}}$  is the vertical unit vector. For a boundary layer of thickness  $H$ , the rate of change of PV scales with the sum of the EBF and the surface buoyancy flux,  $B_0$ :

$$\frac{Dq}{Dt} \sim -\frac{f}{H^2} (\text{EBF} + B_0). \quad (14)$$

Hence, when  $\text{EBF} + B_0 > 0$ ,  $f q$  will be reduced and conditions could become favorable for SI. It is worth emphasizing that the EBF is an *advection* buoyancy flux and that advection does not change the integrated buoyancy. However, the appearance of the EBF in Eq. 14 shows that the EBF is generally associated with a change in the bulk PV. This is due to the fact that a downfront wind stress induces a frictional PV flux that removes PV from the ocean (Thomas, 2005).

As noted above,  $f q < 0$  is a necessary but not sufficient condition for SI and the dominant instability will depend on the Thomas angle. For example, if  $\nabla_h b = 0$  surface cooling ( $B_0 > 0$ ) will decrease  $f q$ , but the flow will become

490 susceptible to gravitational instability (convection) rather than SI. Taylor and Ferrari (2010) used idealized simulations to study buoyancy and wind-driven convection within a frontal zone. They found that like convection, SI acts fast enough to keep the PV close to zero in a ‘low PV layer’. PV conservation then allows a prediction for the deepening of the low PV layer, given the rate of PV destruction due to the surface forcing.

495 Taylor and Ferrari (2010) found that for surface cooling and downfront winds, the low PV layer can be further decomposed into two layers as shown in Figure 8. In a ‘convective layer’, near the surface, stratification is weak, the buoyancy flux is positive, and convective plumes are visible. Note that despite its name, turbulence generated by wind and/or wave breaking can dominate in the ‘convective layer’, and any plumes might be strongly distorted by the associated shear. Below the convective layer, SI develops, resulting in a stable stratification. In this ‘forced SI layer’, small-scale turbulence is generated by secondary shear 500 instabilities that develop between the SI cells. This small-scale turbulence acts in the sense to mix the stable stratification, and hence the buoyancy flux is negative. In the forced SI layer, a cross-front shear (which will be described later) maintains the stable stratification.

505 Taylor and Ferrari (2010) derived a scaling for the depth of the convective layer  $h$ :

$$\frac{|\nabla_h b|^2}{f^2} (B_0 + EBF)^{1/3} h^{4/3} = c \left[ (B_0 + EBF) \left( 1 - \frac{h}{H} \right) \right], \quad (15)$$

510 where  $c \approx 14$  is an empirical scaling coefficient. For a known low PV layer depth,  $H$ , horizontal buoyancy gradient,  $|\nabla_h b|$ , and surface and Ekman buoyancy flux,  $B_0$  and EBF, Eq. 15 can be solved numerically to find  $h$ . This provides a means for identifying when SI will be active under a given set of conditions. At a strong front and/or with weak surface forcing,  $h/H \rightarrow 0$ , and SI will develop throughout the low PV layer. However, when the horizontal buoyancy gradient is weak or forcing is sufficiently strong,  $h/H \rightarrow 1$ , and the low PV layer is expected to be weakly stratified.

515 Taylor and Ferrari (2010) used a turbulent Ekman balance (which is discussed below in Section 0.2.4) to show that the sum of the geostrophic shear production and buoyancy flux in a boundary layer with forced SI is a linear function of depth within the low PV layer, specifically

$$GSP + BFLUX \approx (B_0 + EBF) \left( \frac{z + H}{H} \right). \quad (16)$$

520 Thomas et al. (2013) proposed a model profile for the GSP by further assuming that the buoyancy flux takes the following linear profile within the convective

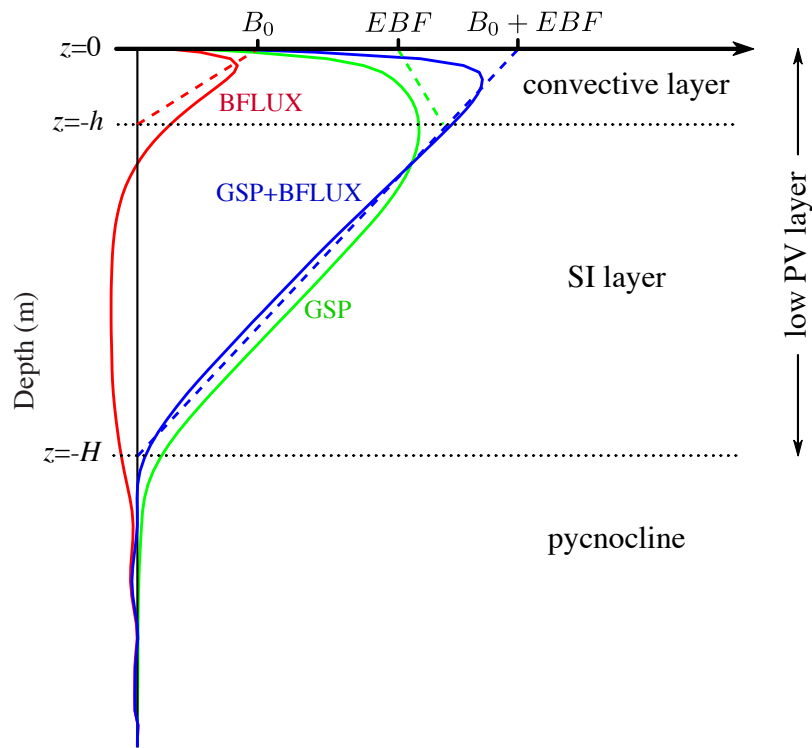


**FIGURE 8** Schematic showing the structure of forced symmetric instability as described by Taylor and Ferrari (2010). Solid curves show the buoyancy flux (BFLUX), geostrophic shear production (GSP), and their sum as calculated from the large-eddy simulation of the response of the Gulf Stream to a storm as reported in Thomas et al. (2016). Dashed lines show the SI parameterization further described in Bachman et al. (2017a). The surface buoyancy flux,  $B_0$ , the Ekman buoyancy flux,  $EBF$ , and their sum are also labeled.

layer:

$$BFLUX \simeq B_0 \frac{z + h}{h}. \quad (17)$$

These model profiles are shown in Figure 8 and compared with the LES in Thomas et al. (2013). Bachman et al. (2017a) used this as a basis for a parameterization for SI and implemented it in the MITgcm.

Observational evidence for SI typically consists of finding of signs of enhanced ventilation, fine-scale interleaving and small-scale mixing within stratified baroclinic fronts. Early suggestions that SI (under the name of ‘slantwise convection’) may be partially responsible for ventilation of the Labrador Current was reported in Straneo et al. (2002). D’Asaro et al. (2011) and Thomas et al. (2013) observed regions with  $f q < 0$  in the Kuroshio and Gulf Stream fronts, respectively. D’Asaro et al. (2011) and Thomas et al. (2016) observed elevated dissipation rates within these regions, providing indirect evidence for geostrophic shear production associated with SI.

Several studies from the OSMOSIS project have shown evidence for SI in the subtropical northeast Atlantic. Using a full year of glider and mooring observations, Thompson et al. (2016); Buckingham et al. (2019); Yu et al. (2020) found a stratified low PV layer in the winter with scalings that were consistent with the model and theory in Taylor and Ferrari (2010). Yu et al. (2019b) found evidence for wind-forced SI at a transient front in the same region, as illustrated in Fig. 9. In-situ observations from the mooring array were used to compute the vertical stratification, the lateral buoyancy gradient, and the most likely instability (GI,SI,II) according to the classification described in Fig. 7. The mixed layer was favorable to GI triggered by atmospheric cooling ( $\sim 200 \text{ W m}^{-2}$ ) between 3 and 7 April 2013, which resulted in a deepening of the mixed layer down to almost 300 m. A strong lateral buoyancy gradient, generated by the confluence of mesoscale eddies, developed between 8 and 11 April 2013. Persistent down-front winds during this period led to the generation of SI (Fig. 9c) and an EBF  $\sim 650 \text{ W m}^{-2}$ . The SI event was also associated with elevated glider-derived turbulent dissipation rates. Other evidence of SI were found by Ramachandran et al. (2018) in a shallow front in the Bay of Bengal, by Peng et al. (2020) in a density filament in the Benguela upwelling system, and by Koenig et al. (2020) in a thermohaline front caused by sea ice melt in the Nansen Basin. Together these studies suggest that SI does not require strong climatological fronts like the Gulf Stream and Kuroshio, and instead can occur in typical open ocean conditions.

Perhaps the most direct evidence for SI comes from observations of its influence on temperature and tracer. Saveliev et al. (2018) observed step-like patterns in the surface temperature in the southern Gulf Stream from airborne thermal imagery. These features closely resemble the feature seen in numerical simulations of SI (e.g., Stamper and Taylor, 2017) and concurrent ship-based measurements confirmed that conditions were favorable for SI. Wenegrat et al. (2020) analyzed a tracer release experiment conducted in the Gulf Stream during

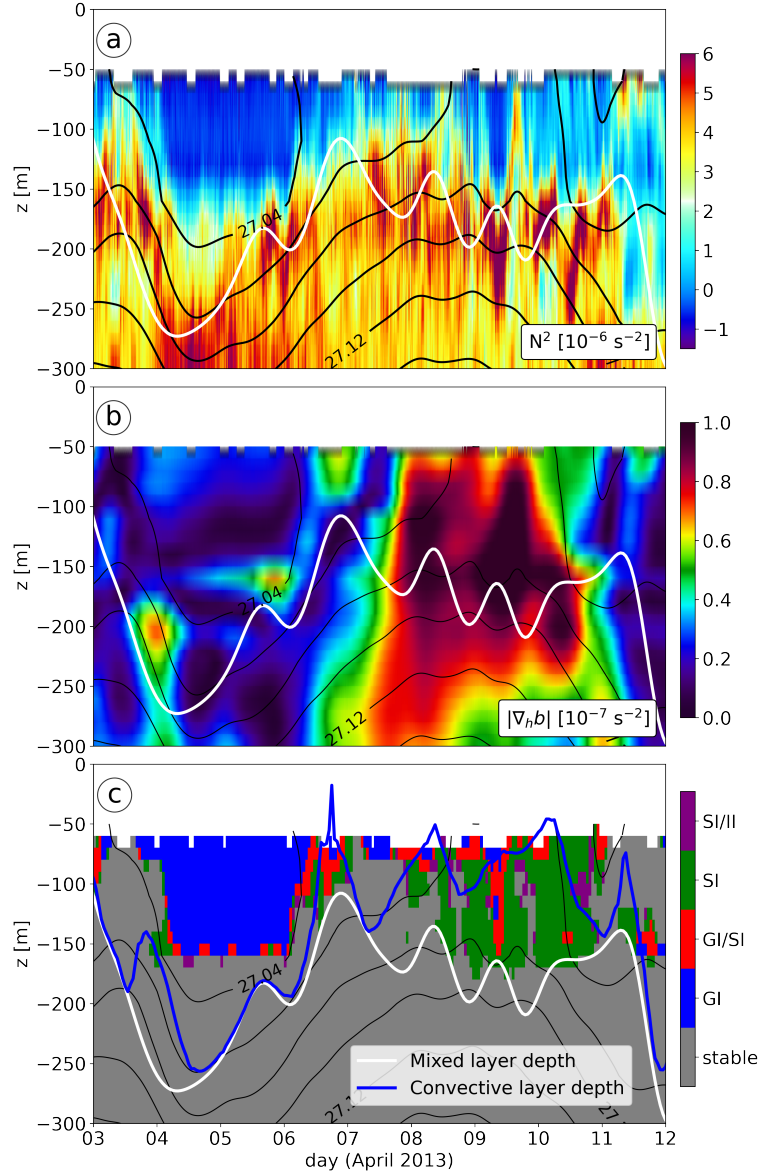


**FIGURE 9** Time series of (a) vertical buoyancy stratification  $N^2$ , (b) lateral buoyancy gradient  $|\nabla_h b|$ , and (c) submesoscale instability category at the OSMOSIS central mooring site from 3 to 12 April 2013. The white line indicates the mixed layer depth and the blue line indicates the convective layer depth. Isopycnals are overlaid as black contours at intervals of  $0.02 \text{ kg m}^{-3}$ . Adapted from Yu et al. (2019b).

565 a period with strong wind forcing and near-inertial oscillations. The observations and numerical simulations suggest that circulation associated with SI mixed the dye along isopycnals. This, combined with episodic vertical mixing associated with near-inertial shear led to significant cross-front mixing of the tracer due to shear dispersion.

570 A global view of the scale and relative likelihood of SI, as computed by Dong et al. (2021), is provided in Fig. 6. The most unstable wavelength for SI ( $L_{SI}$ ) is estimated from Stone (1966)'s linear prediction applied to the upper ocean state extracted from the global submesoscale-permitting LLC4320 simulation. The SI scale varies strongly with latitude, with median values of 1.5 km at the equator to 15 m at high latitudes. It also varies with seasons as the median scale roughly doubles in winter compared to summer. The SI scales are 1 or 2 orders of magnitude smaller than the MLI scale, and basin or global-scale models do 575 not yet have sufficient resolution to capture SI.

### 0.2.3 Submesoscale processes at the bottom of the ocean

Fronts can also form at the bottom of the ocean. This has been widely studied for 580 application in coastal areas. Typically, over a continental shelf, the alongshore winds in the presence of a cross-shelf density gradient can create upwelling or downwelling situations. In the upwelling case, which has been the most studied (Barth, 1989a,b, 1994; Durski and Allen, 2005), the surface front leads to the same type of baroclinic instability or symmetric instability as described previously. However, in the case of downwelling, a density front intersects the 585 bottom rather than the surface. This can lead to baroclinic instability as well, generating an eddy field with the same typical scale (1 - 10 km) (Brink, 2016).

Submesoscale currents and fronts are also found in deeper parts of the ocean, especially in the presence of steep topography such as seamounts and ridges. For example, energetic submesoscale currents are visible near the Mid-Atlantic 590 Ridge in Fig. 3. The corresponding kinetic energy spectra exhibit a shallow  $\sim k^{-2}$  slope, contrasting with open-ocean – i.e., far from topographic features – regimes of turbulence, dominated by mesoscales and a  $\sim k^{-3}$  slope (Vic et al., 2018).

The bottom boundary layer (BBL) of the ocean exhibits key similarities with 595 the surface boundary layer. Available potential energy associated with horizontal buoyancy gradients in the BBL can feed an equivalent of MLI (Wenegrat et al., 2018a). Friction and diapycnal mixing at the bottom can also inject or destroy PV in the BBL (Benthuyse and Thomas, 2012; Morel et al., 2019), which can either stabilize it or trigger a variety of unbalanced submesoscale instabilities like 600 symmetric or centrifugal (inertial)<sup>8</sup> instabilities (Allen and Newberger, 1998;

---

8. Here we use the term ‘centrifugal instability’ synonymously with ‘inertial instability’ (as defined in Section 0.2.2.2) since the former has become the standard convention in studies of the BBL (McWilliams, 2016)

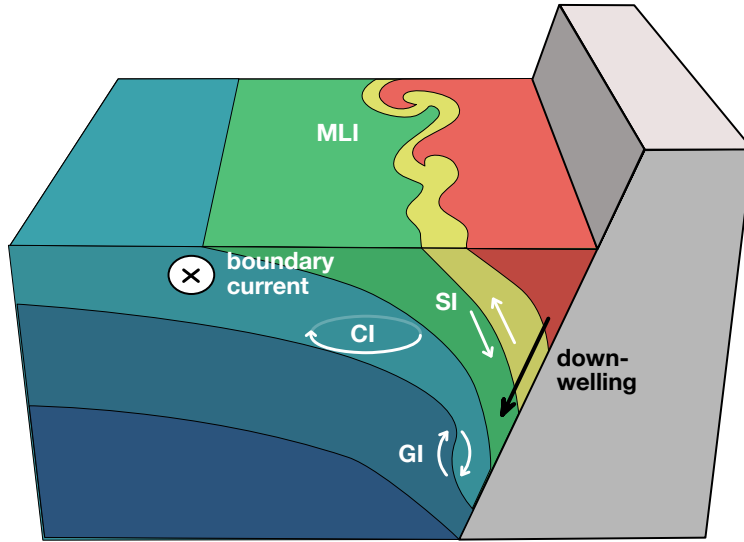


**FIGURE 10** Idealized depiction of various submesoscale processes in the bottom boundary layer. A boundary slope current moving in the direction of Kelvin wave propagation generates a downslope Ekman current. After loss of potential vorticity due to friction and diapycnal mixing at the bottom, the front can be unstable to gravitational instability (GI), symmetric instability (SI), or centrifugal instability (CI). Submesoscale eddies develop through baroclinic instability of the bottom mixed-layer (MLI). Schematic adapted from Naveira Garabato et al. (2019).

Molemaker et al., 2015; Dewar et al., 2015). The frictional drag can play the same role as the wind in the upper ocean and lead to forced instability regimes (Wenegrat and Thomas, 2020). Thus, most of the submesoscale instabilities described in Section 0.2.2 in the surface layer have a counterpart at the bottom as summarized in Fig. 10 and described below.

#### 0.2.3.1 Bottom boundary layer baroclinic instability

A counterpart to MLI occurs in weakly stratified boundary layers over sloping topography (Brink, 2012, 2013; Wenegrat et al., 2018a). The problem of baroclinic instability over a slope is a classic one (Blumsack and Gierasch, 1972; Mechoso, 1980; Solodoch et al., 2016), which has recently been revisited for buoyancy-driven flow by Hetland (2017) and for baroclinic instability over the continental shelf by Chen et al. (2020). It has also been used for low  $Ri$  regimes characteristics of the BBL by Wenegrat et al. (2018a).

The model is similar to the Eady model presented in Sec. 0.2.2.1, with the addition of a topographic slope  $\theta$ . The ratio of the topographic slope to minus

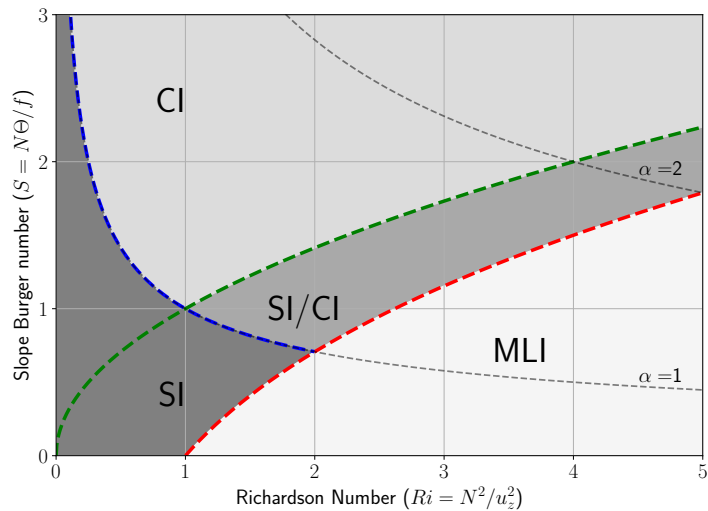


**FIGURE 11** Regime diagram for submesoscale baroclinic instability (MLI), symmetric instability (SI), centrifugal instability (CI), and mixed instability (SI/CI) in the ocean BBL as a function of the Richardson number  $Ri = N^2/u_z^2$  and the slope Burger number  $S = N\Theta/f$ . The dashed red line shows the limit of zero PV, the dashed green line shows the limit of zero absolute vorticity  $f + \zeta = 0$ , and the dashed blue line is the theoretical expectation for the ratio of lateral and vertical shear production  $LSP/GSP = 1$  in the hydrostatic limit. Adapted from Wenegrat et al. (2018a).

the isopycnal slope is then given by the slope parameter:

$$\alpha = \frac{N^2}{fu_z} \theta = SRi^{\frac{1}{2}} \quad (18)$$

where:

$$S = \frac{N\theta}{f} \quad (19)$$

is the slope Burger number and  $Ri$  is the Richardson Number. As in Hetland (2017) and Wenegrat et al. (2018a),  $\alpha = 1$  corresponds to an isopycnal slope equal and opposite to the topographic slope and  $\alpha = -1$  to isopycnals parallel to the topography. With uniform background vertical stratification and slope-normal shear, the effect of the topographic slope is to stabilize baroclinic instability for  $\alpha < -1$  (Blumsack and Gierasch, 1972).

Realistic BBL structures have been shown to support submesoscale baroclinic instability (Wenegrat et al., 2018a). A first case corresponding to a BBL generated by bottom-intensified mixing supports a baroclinic instability that restratifies the thick outer layer of the BBL. A second case, corresponding to an interior flow in the direction of Kelvin wave propagation (meaning that the flow has the coast on its right in the Northern Hemisphere), drives a downslope Ekman flow and generates available potential energy that also feeds a submesoscale baroclinic instability. In most BBL cases, the isopycnals intersect the bottom almost perpendicularly, corresponding to a positive  $\alpha$ , such that small positive values of  $\alpha$  and  $S$  might be the most common configuration in the BBL (Wenegrat et al., 2018a).

The most unstable bottom MLI wavelength ( $L_{BMLI}$ , Fig. 6c,d) has also been estimated globally by Dong et al. (2020b), following the same methodology than for MLI in the surface layer (See section 0.2.2.1). The median values are in the order of  $O(1)$  km, thus slightly smaller than the surface MLI scales and well into submesoscales.

### 0.2.3.2 Bottom injection of PV and submesoscale instabilities

Friction and diapycnal mixing at the bottom are strong sources of PV (Benthuyzen and Thomas, 2012; Molemaker et al., 2015; Gula et al., 2015b). PV is extracted in the case of a boundary slope current moving in the direction of Kelvin wave propagation because the frictional drag reduces velocity along the slope, induces a negative horizontal velocity shear and a downslope Ekman flow that advects lighter water under denser water and drives diabatic mixing. PV is increased when the current is in the opposite direction (meaning that the flow has the coast on its left in the Northern Hemisphere) when it leads to a positive horizontal velocity shear and an upslope Ekman advection that tends to restratify the bottom boundary layer (Benthuyzen and Thomas, 2012).

The PV extraction related to downslope buoyancy advection is a close analogous of the PV extraction in the surface layer in the case of a downfront wind,

as described in subsection 0.2.2.3. The advection of lighter water under denser water can generate convective mixing, which acts to increase the horizontal buoyancy gradient and decrease the vertical gradient, and can lead to a regime of forced SI or centrifugal (inertial) instability (CI) (Allen and Newberger, 1998; Molemaker et al., 2015; Dewar et al., 2015; Jiao and Dewar, 2015; Gula et al., 2016; Yankovsky and Legg, 2018; Wenegrat et al., 2018a; Wenegrat and Thomas, 2020; Naveira Garabato et al., 2019).

As in the surface layer, these additional instabilities (GI, SI and CI/II) appear in the linear stability analysis of the Eady model when ageostrophic perturbations are included. The stability analysis for a geostrophically balanced along-slope flow in the direction of Kelvin wave propagation, with uniform stable stratification and uniform slope-normal velocity shear, is illustrated in Fig. 11 based on the scalings derived in Wenegrat et al. (2018a). When the slope Burger number is small, the criterion for instability is similar to that in the surface layer, namely SI is dominant for  $Ri \lesssim 1$  and MLI is dominant for  $Ri \gtrsim 1$ . When the slope Burger number is increased, the dominant mode becomes CI or a mixed SI/CI mode at moderate  $Ri$ , and the baroclinic instability mode is shifted to larger  $Ri$ .

The different types of instabilities occurring when the PV is negative can be identified using the same criteria as in the surface layer (Sec. 0.2.2.2). In particular, instabilities can be classified based on their dominant source of energy: GI extract their energy predominantly from buoyancy flux (*BFLUX*), SI – from geostrophic shear production (*GSP*), and CI – from lateral shear production (*LSP*) terms. The limit between the CI and SI regimes in the stability diagram (Fig. 11) corresponds to the ratio of lateral and vertical shear production being equal to 1 (*LSP/GSP* = 1), which gives the condition  $\alpha = 1$  in the hydrostatic limit (see Equ. 33 in Wenegrat et al., 2018a).

Recent high-resolution observations taken in an abyssal boundary current flowing along steep topography in the Orkney Passage highlighted the generation of GI, SI and CI in a configuration corresponding to a downslope Ekman flow (Fig. 12, Naveira Garabato et al. 2019). GI is dominant in a  $\approx 100$  m thick layer over the bottom, while SI and CI happen over a larger region, which is about 1–2 km high and 500 m wide, as shown in Fig. 12. These instabilities generate an intensified near-boundary turbulence and drive buoyancy exchanges between the boundary layer and the interior.

### 0.2.3.3 Topographic wakes

A feature specific of the bottom is that, in the presence of a slope, it is possible for the highly sheared flow in the BBL to separate from the boundary and move into the stratified interior of the ocean, thus forming turbulent topographic wakes (Molemaker et al., 2015; Gula et al., 2015b, 2016), which can be even more efficient at driving diapycnal mixing. If the boundary is horizontal, which happens in the surface mixed-layer or over a flat bottom, the frictional drag can only induce a vertical velocity shear, such that the flow only acquires horizontal

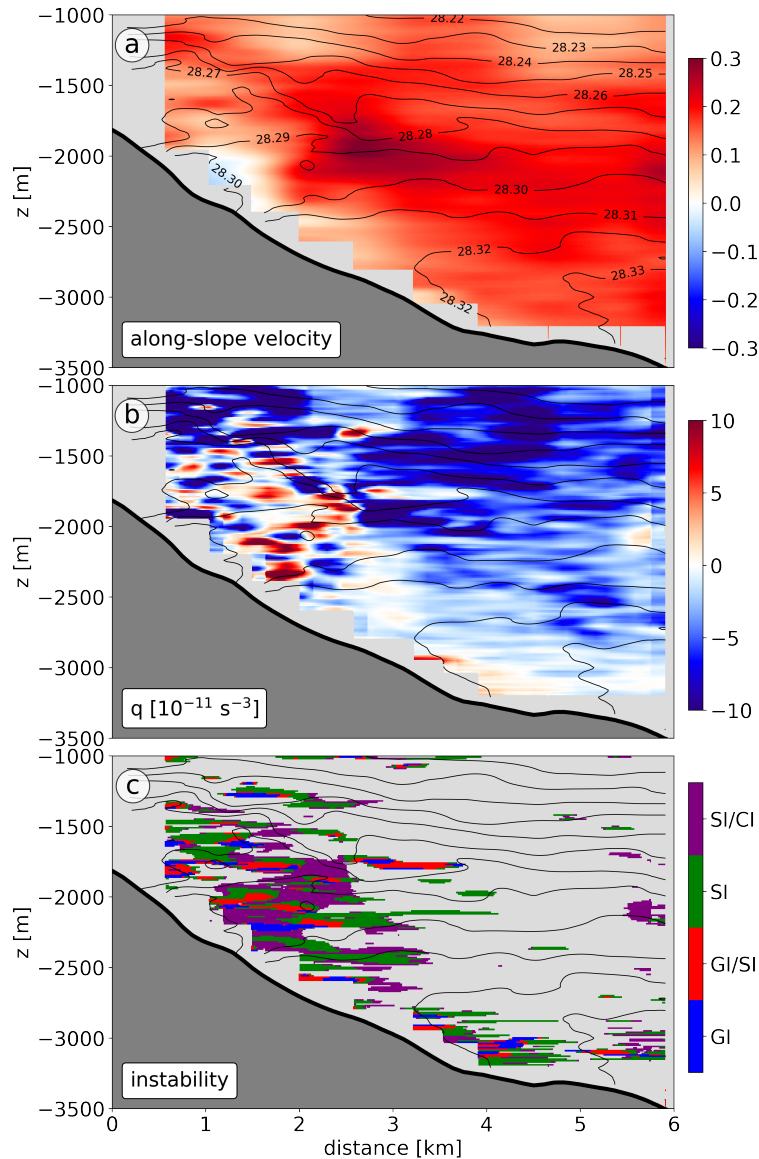


**FIGURE 12** Transect across an abyssal boundary current near the Orkney Passage sill (section B3 in Naveira Garabato et al. (2019)). (a) Along-slope velocity (color) and neutral density (in  $\text{kg m}^{-3}$ , black contours). (b) PV (color) and neutral density (black contours). (c) Instability type (color) and neutral density (black contours). Adapted from Naveira Garabato et al. (2019).

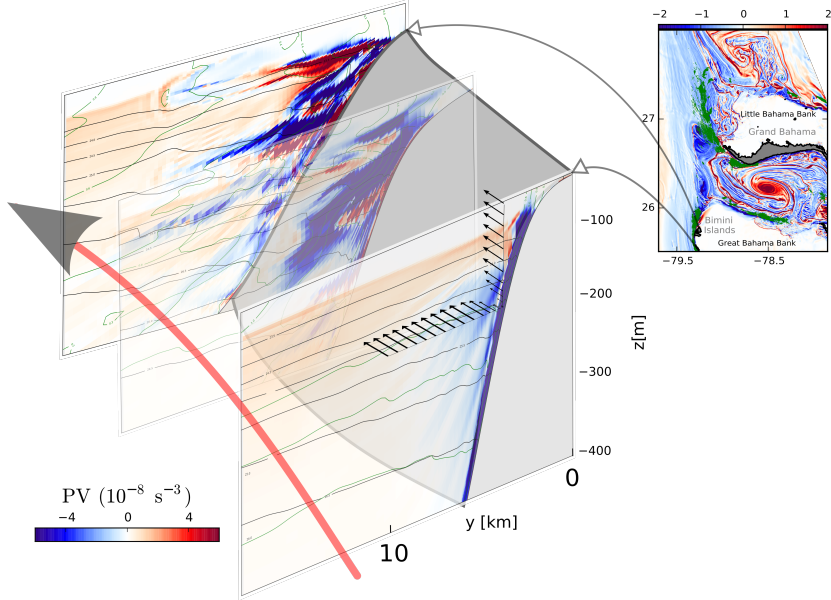


**FIGURE 13** Snapshots of potential vorticity (PV, in  $10^{-8} \text{ s}^{-3}$ ) along the Bahamas Banks showing generation of negative PV (in colors) along the slope and the onset of centrifugal instability in the wake. The big red arrow indicates the direction of the Gulf Stream, and the small black arrows the velocity vectors close to the slope. Density is shown in black contours with an interval of  $0.5 \text{ kg m}^{-3}$  and along-slope velocity is shown in green contours with an interval of  $0.2 \text{ m s}^{-1}$ . The inset on the right shows the instantaneous surface relative vorticity  $\zeta = v_x - u_y$ , normalized by  $f$  (in colors), with regions of high kinetic energy dissipation (depth-integrated energy dissipation  $\langle \epsilon \rangle > 2 \times 10^{-4} \text{ W m kg}^{-1}$ ) highlighted in green. Adapted from Gula et al. (2016).

vorticity. It is thus unlikely to separate from the boundary as vertical motions are strongly limited by rotation and stratification, and instabilities and turbulence mostly stay inside the BBL (McWilliams, 2017). However, over a sloped bottom, the topographic drag induces both a vertical and a horizontal velocity shear, and the sheared layer has the capability of separating from the boundary either due to the geometry of the boundary (Molemaker et al., 2015) or due to the background mesoscale straining (Vic et al., 2015). Escaping the constraint of the boundary, the sheared flow triggers instabilities such as CI/SI or horizontal shear instabilities that lead to elevated local dissipation and mixing in the stratified interior (Gula et al., 2016) and to the generation of submesoscale coherent vortices (SCV) (Molemaker et al., 2015; Perfect et al., 2018; Srinivasan et al., 2019), which can further export tracers and water masses over much longer time and distances (Gula et al., 2019).

A typical case corresponds to a flow past a seamount, which may generate a turbulent topographic wake with both cyclonic and anticyclonic vorticity, leading

to instabilities and formation of coherent vortices in the wake of the seamount, as seen from idealized (Perfect et al., 2018; Srinivasan et al., 2019) or realistic simulations (Srinivasan et al., 2017; Gula et al., 2019; Napolitano et al., 2021). There are similarities with the more classical island wake, which forms as a von Karman street with alternating cyclones and anticyclones (Stegner, 2014).

Vorticity is similarly generated when a current flows along sloped topography. The vorticity may be cyclonic or anticyclonic depending on the orientation of the current relative to the topography. For example, the Gulf Stream along the U.S. seaboard generates cyclonic vorticity. There, the topographic drag amplifies the horizontal cyclonic shear of the jet until the current separates from the slope. The highly sheared flow becomes unstable to barotropic shear instability, which leads to the formation of streets of submesoscale vortices as described in Gula et al. (2015a,b).

The anticyclonic case is particularly interesting as it can trigger CI, which has a strong impact on energy dissipation and mixing (Dewar et al., 2015; Gula et al., 2016). Following the sequence of processes described in the context of the California Undercurrent (Molemaker et al., 2015) or the Gulf Stream (Gula et al., 2016), relative vorticity can locally become much less than  $-f$  and result in negative PV. The slope has a stabilizing effect upstream of separation, but the negative PV strip leads to intense CI and energy dissipation in the separated wake (see Fig. 13). In a Gulf Stream model, the vertically integrated dissipation rates of eddy kinetic energy due to parameterized turbulence (KPP), reach values up to  $8 \times 10^{-4} \text{ W m kg}^{-1}$  instantaneously at  $26^\circ\text{N}$  following separation of the negative PV strip from the slope. It is of the same order as the dissipation rates observed in an intense surface front within the Kuroshio Current (D'Asaro et al., 2011) integrated over the mixed-layer.

Equatorial topographic wakes are particularly efficient at dissipating energy (Srinivasan et al., 2021). The background rotation is important to drive the merging and alignment of vorticity structures in the wakes. However, in the tropics, the decreasing  $f$  leads to more vertically-sheared wake structures and increasing energy dissipation.

Topographic wakes are a common feature in realistic submesoscale-resolving simulations, and most of the studies on the subject come from idealized or numerical simulations (McWilliams, 2016). It remains very complicated to sample such localized events of turbulence in the ocean, especially in the deep regions. Intense small-scale turbulence and the formation of submesoscale eddies have been observed in the wake of the Palau island chain, in the western Pacific, during the program FLEAT (See articles in the special issue of Oceanography on the subject: Johnston et al., 2019; MacKinnon et al., 2019). Direct observations of turbulent wakes in the deep ocean are needed to better quantify the impact of these processes. Deep seamounts and steep topographic features are numerous and the cumulative impact of topographic wakes on mixing might still be strongly underestimated.

### 0.2.4 The influence of vertical mixing on the evolution of a submesoscale front

755

In this section we will discuss the influence of small-scale turbulence and vertical mixing on the evolution of submesoscale fronts and thereby the submesoscale currents within. Study of these multi-scale interactions is at a relatively early stage and many open questions remain. Here, we discuss some of the advances that have been made in this area. We start by discussing the ageostrophic circulation in ‘generalized Ekman’ (GE) or ‘turbulent thermal wind’ (TTW) balance, driven by vertical mixing of momentum at fronts, emphasizing the connections between these balance relations. We then discuss the role that a GE/TTW balanced flow plays in the evolution of a front. Finally, we discuss the connection between GE/TTW balance and submesoscale instabilities.

760

As noted in Chapter 4, when averaged over a sufficiently long period of time, the wind-driven currents in a horizontally homogeneous mixed layer sufficiently far from the equator are expected to be in a state of turbulent Ekman balance, (e.g., Cushman-Roisin and Beckers, 2011):

765

$$-f \langle v^a \rangle = -\frac{d}{dz} \langle u' w' \rangle = \frac{d}{dz} \left( \nu_T(z) \frac{d \langle u^a \rangle}{dz} \right), \quad (20)$$

$$f \langle u^a \rangle = -\frac{d}{dz} \langle v' w' \rangle = \frac{d}{dz} \left( \nu_T(z) \frac{d \langle v^a \rangle}{dz} \right), \quad (21)$$

where superscript  $a$  denotes the ageostrophic velocity, angle brackets denote a time (and/or horizontal) average, and  $\nu_T$  is a turbulent viscosity which is assumed to be horizontally isotropic. The solution to these equations yields the classical Ekman spiral (Ekman, 1905), albeit modified by the depth-dependence of the turbulent viscosity. This balance has been confirmed with observations, although this requires a careful analysis and a long time average (Price et al., 1987; Lenn and Chereskin, 2009; Polton et al., 2013; Johnson et al., 2020a).

770

In classical turbulent Ekman balance, the geostrophic velocity (which was implicitly cancelled with the pressure gradient in Eqns. 20-21) is assumed to be depth-independent, and hence only the ageostrophic shear appears in the last term in each equation. At a front, however, the geostrophic flow also includes a vertical shear. The vertically-sheared geostrophic flow,  $\mathbf{u}_g(z)$ , can be mixed vertically by small-scale turbulence, thereby driving an ageostrophic response. In the context of wind-driven flow at fronts in the Tropical Pacific, Cronin and Kessler (2009) derived what they termed the ‘generalized Ekman’ balance, which

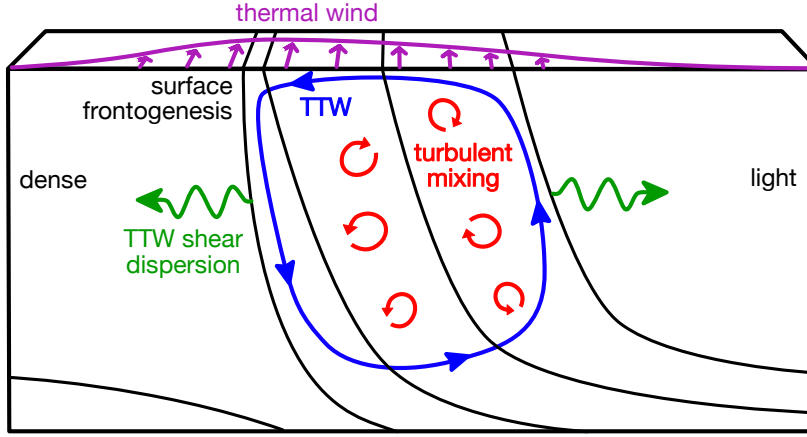


**FIGURE 14** Schematic of the cross-front turbulent thermal wind (TTW) circulation and its influence on the evolution of submesoscale fronts. Near the surface, convergent cross-front TTW circulation leads to frontogenesis as described in McWilliams et al. (2015); McWilliams (2017). Re-stratification by the TTW circulation and vertical mixing leads to frontolysis through shear-dispersion as described in Crowe and Taylor (2018, 2019).

can be written

$$-f \langle v \rangle = -\frac{1}{\rho_0} \left\langle \frac{\partial p}{\partial x} \right\rangle + \frac{d}{dz} \left( v_T(z) \frac{d \langle u \rangle}{dz} \right), \quad (22)$$

$$f \langle u \rangle = -\frac{1}{\rho_0} \left\langle \frac{\partial p}{\partial y} \right\rangle + \frac{d}{dz} \left( v_T(z) \frac{d \langle v \rangle}{dz} \right), \quad (23)$$

$$\frac{1}{\rho_0} \left\langle \frac{\partial p}{\partial z} \right\rangle = \langle b \rangle. \quad (24)$$

Note that the full velocity,  $\mathbf{u} = \mathbf{u}_g + \mathbf{u}_a$ , appears in the Coriolis and vertical mixing terms. Wenegrat and McPhaden (2016) found analytical solutions to Eqns. 22-24 and extended the model to include the influence of surface waves, while Taylor and Ferrari (2010) found that this balance holds during forced symmetric instability (with the vertical momentum flux terms instead of a turbulent viscosity).

Alternatively, Eqns. 22-24 can be viewed as a generalization of thermal wind balance. Gula et al. (2014) note that when vertical mixing of momentum is included in a state that is otherwise in geostrophic and hydrostatic balance, the vertical shear satisfies the following equations

$$-f \frac{d \langle v \rangle}{dz} = - \left\langle \frac{\partial b}{\partial x} \right\rangle + \frac{\partial^2}{\partial z^2} \left( v_T \frac{\partial \langle u \rangle}{\partial z} \right), \quad (25)$$

$$f \frac{d \langle u \rangle}{dz} = - \left\langle \frac{\partial b}{\partial y} \right\rangle + \frac{\partial^2}{\partial z^2} \left( v_T \frac{\partial \langle v \rangle}{\partial z} \right). \quad (26)$$

Gula et al. (2014) called this ‘turbulent thermal wind’ (TTW) balance and they found that this described the circulation in simulations of submesoscale cold filaments in the Gulf Stream.

785

Note that Eqns. 25-26 can be obtained by taking the vertical derivative of Eqns. 22 and 23 and using 24. With a constant turbulent viscosity, Charney (1973) showed that this is the leading order balance in the hydrostatic Boussinesq equations for small Rossby number and Crowe and Taylor (2018) showed that the same analysis can be extended to include a depth-dependent turbulent viscosity. Garrett and Loder (1981) and Ponte et al. (2013) discussed the use of Eqns. 25-26 to diagnose the circulation for given a density field and  $v_T(z)$  and showed that simple solutions can be obtained in the limit of small Ekman number (i.e. weak vertical mixing) where the geostrophic shear can be used in the viscous terms. Finally, the dynamical balance underlying TTW is the same as the leading order balance in the subinertial mixed layer (SML) model of Young (1994).

790

795

Unlike the inviscid thermal wind balance, TTW balance is associated with a vertically-sheared cross-front flow. A simple explanation for this cross-front flow is as follows. Consider starting with a front in thermal wind balance. Then, suppose that small-scale turbulence (*e.g.*, convection driven by surface cooling) leads to vertical mixing which reduces the along-front shear. Since the mixed layer depth is typically much smaller than the width of fronts, isotropic mixing by small-scale turbulence will not have a strong direct influence on the horizontal density gradient. As a result, the hydrostatic pressure gradient will also be relatively unaffected by small-scale mixing. Therefore, a reduction in the along-front shear by vertical mixing will lead to an unbalanced cross-front pressure gradient which will, in turn, drive a cross-front flow. The cross-front flow associated with this mechanism will always be in the sense to re-stratify the front with light water advected over dense water. The TTW circulation is also associated with a surface PV flux at submesoscale fronts which may dominate both wind and surface buoyancy-flux-driven PV fluxes. These effects have been shown to modify the seasonal cycle of mode water formation in the Gulf Stream (Wenegrat et al., 2018b).

800

805

810

815

815

The cross-front GE/TTW flow can influence the evolution of the front and the associated submesoscale instabilities. This represents a mechanism whereby vertical mixing by small-scale turbulence can influence submesoscales (Garrett and Loder, 1981; Thompson, 2000). As discussed in Garrett and Loder (1981), the unbalanced pressure gradient and hence the cross-front flow will tend to be largest at the location where the horizontal density gradient is maximum and

820 the cross-front flow will naturally tend to zero outside the front. As sketched in Figure 14, the horizontal convergence/divergence of the TTW circulation will lead to downwelling on the dense side of the front and upwelling on the light side of the front. Near the surface on the dense side of the front, the convergence of the TTW flow will lead to frontogenesis. McWilliams et al. (2015) and Sullivan and McWilliams (2018) show that this leads to a rapid collapse of outcropping dense filaments (where the TTW circulation consists of two counter-rotating cells with downwelling in the center of the dense filament). McWilliams (2017) developed a diagnostic framework which combined the TTW circulation with the Omega equation to analyze the secondary circulation and frontogenetic tendency 825 for fronts and filaments. Bodner et al. (2019) used a perturbation approach to investigate the influence of horizontal and vertical mixing on the evolution of a front based on the inviscid frontogenetic model described in Shakespeare and Taylor (2013). A diurnal modulation of the small-scale turbulence, driven by the solar cycle, has been shown to drive a diurnal modulation cycle of frontogenesis 830 and relaxation (Dauhajre and McWilliams, 2018), which can be described using transient turbulent thermal wind (T3W) equations.

835 As discussed in Garrett and Loder (1981), Young (1994), and Crowe and Taylor (2018), the vertically-sheared cross-front TTW circulation can cause the width of the front to increase through shear dispersion (*e.g.*, Young and Jones, 1991). As the cross-front circulation slumps the isopycnals, small-scale 840 turbulence mixes density vertically, and the sustained combination of these two processes leads to an increase in the frontal width and a spindown of the front. When the turbulent viscosity depends only on  $z$ , Crowe and Taylor (2018) found that surface-intensified frontogenesis occurs during a brief transient phase before 845 the front spreads through shear dispersion. They also found that as the front spreads, it limits to a self-similar shape with a roughly constant horizontal density gradient in the interior of the front. At the edges of the front, intense narrow bands of upwelling and downwelling appear in analytical solutions (Crowe and Taylor, 2018) and numerical simulations (Crowe and Taylor, 2019). Crowe and Taylor (2020) extended this work to include the circulation driven by a surface 850 wind stress and a surface buoyancy flux and identified the conditions when the front sharpens or spreads.

855 Most of the studies referenced above represent vertical mixing using a prescribed turbulent viscosity (*e.g.*, Crowe and Taylor, 2018), a simple model for mixing (*e.g.*, Young, 1994), or a boundary layer parameterization (such as the KPP scheme) (*e.g.*, Gula et al., 2014; McWilliams et al., 2015). Although large-eddy simulations have shown that turbulent mixing can be significantly modified at submesoscale fronts (*e.g.*, Taylor, 2016; Smith et al., 2016), much less is understood about how turbulence reacts and couples with the evolution 860 of submesoscale fronts. One notable exception is Sullivan and McWilliams (2018) who studied large-eddy simulations of a collapsing submesoscale cold filament. Small-scale turbulence was generated in their simulations by wind forcing and/or surface cooling. Turbulence triggered the collapse of the filament

865 through GE/TTW-induced frontogenesis. However, in the later stages of the filament evolution, this frontogenesis is arrested by enhanced turbulence generated through horizontal shear instabilities, as further discussed in Sec. 0.2.5.

870 There are many open questions related to the interactions between submesoscale fronts and turbulent mixing. For example: Does the suppression of vertical mixing following frontal re-stratification (Taylor and Ferrari, 2011) enhance or inhibit TTW-induced frontogenesis? How is the spreading of a front by shear-dispersion changed when turbulence is modified by frontal shear/stratification? What factors influence the arrest of frontogenesis by turbulence and hence equilibrium frontal widths? One of the major challenges in this area is the computational cost associated with simulations that capture both changes to small-scale turbulence and the evolution of submesoscale fronts. For example, the simulations in Sullivan and McWilliams (2018) used  $\sim 10^{10}$  grid points. However, advances in computing power should make these simulations more accessible, and will allow an exploration of parameter space that will likely be necessary to develop and test parameterizations of these processes.

### 880 0.2.5 Frontal arrest and routes to dissipation

885 The theory of frontogenesis does not explain how the sharpening of the front is ultimately stopped. As noted above, inviscid theory predicts the formation of a discontinuity in the surface density in a finite time (Hoskins and Bretherton, 1972). In reality the sharpening of the front can be arrested due to spatio-temporal variability of the large-scale flow (McWilliams et al., 2019), dissipation by intensified small-scale turbulence or an instability and eddy-feedback equilibration process. Frontal arrest due to the effect of baroclinic instability has been shown in McWilliams and Molemaker (2011). Another likely scenario is the triggering of horizontal shear instability (Gula et al., 2014; Samelson and Skillingstad, 2016; Sullivan and McWilliams, 2018; Verma et al., 2019), which has growth rates scaling with the cross-front velocity gradient. This scenario for frontal arrest has been confirmed using large-eddy simulations of an idealized dense filament by Sullivan and McWilliams (2018). Within less than a day, frontogenesis is arrested at a small width ( $\approx 100$  m), primarily by an enhancement of the turbulence through a small submesoscale, horizontal shear instability of the sharpened filament, followed by a subsequent slow decay of the filament by further turbulent mixing. However, other studies have found sharpening of a front down to  $O(10)$  m until the release of a gravity current (Pham and Sarkar, 2018).

900 Submesoscale processes can thus initiate a forward cascade of energy and tracer variance, ultimately leading to energy dissipation and diapycnal mixing in frontal regions. Evidence of such a forward cascade of energy to dissipative scales has been observed at isolated small-scale frontal features in idealized high-resolution numerical simulations of MLI (Molemaker et al., 2010; Skillingstad and Samelson, 2012; Samelson and Skillingstad, 2016). Quanti-

tative assessments in submesoscale-permitting realistic model have confirmed that the forward cascade of kinetic energy at the smallest resolved scales of the models occurs mainly in frontogenetic regions (Schubert et al., 2020), and that superinertial ageostrophic motions play an important role (Ajayi et al., 2021).  
910 However, the submesoscale energy cascades have also been shown to be strongly time and region dependent (Yang et al., 2021).

Very high levels of turbulent kinetic energy dissipation have been observed at strong persistent fronts like the Kuroshio or Gulf Stream (Nagai et al., 2009; D'Asaro et al., 2011; Nagai et al., 2012). In the open-ocean, on the other hand,  
915 the contribution of submesoscale processes to small-scale turbulence may seem weak compared to the contribution of winds and waves, as observed during the OSMOSIS campaign (Buckingham et al., 2019), but they still have an important impact for extracting energy from the geostrophic circulation. Observations of a front in the Baltic Sea, following the passage of a storm, have also highlighted a  
920 direct route to turbulent dissipation, linked to shear instability (Carpenter et al., 2020). Another observation of a density filament in the Benguela upwelling system also confirmed high level of energy dissipation driven by forced SI Peng et al. (2020).

### 0.3 REDISTRIBUTION OF DENSITY AND RESTRATIFICATION AT THE SUBMESOSCALE

Submesoscale instabilities tend to reduce horizontal density gradients and enhance vertical density gradients – i.e., they are restratifying in nature. The reason is twofold: Some of these instabilities tap into the available potential energy associated with lateral density gradients directly, while others draw kinetic energy from currents, disrupt the thermal wind balance, and force the lateral gradients to adjust. This results in ageostrophic secondary circulations that act to restratify the flow on time scales of hours to weeks. The stratification of the upper-ocean is thus controlled by the competing effects of vertical mixing and restratification.  
930 The relative importance of these two processes is important in determining the density structure of the upper ocean.

In this section, we first describe separately the effect of the different submesoscale processes presented in Sec. 0.2 on the restratification of the ocean. Then, we comment on the competition between the different type of processes and their overall importance in the ocean.  
935

#### 0.3.1 Restratification induced by submesoscale processes

Submesoscale processes can increase vertical stratification on time scales that compete with surface radiative forcing. Submesoscale restratification is usually quantified in terms of the horizontal  $u'b'$  or vertical buoyancy flux  $w'b'$ , which correspond to a redistribution of density, but are often expressed as an equivalent surface heat flux to facilitate comparison with the ubiquitous restratification due  
940

to surface heat fluxes and freshwater input.

Earlier works on submesoscale frontal slumping have highlighted the role of geostrophic adjustment (Tandon and Garrett, 1994) and of the ASC associated with surface frontogenesis (Lapeyre et al., 2006) to restratify the horizontal gradients generated by wind mixing and the straining of mesoscale eddies. In this case, the vertical buoyancy flux associated with strain-induced frontogenesis of a single front scales as  $w'b' \sim H^2|\nabla_h b|/f^2$  (McWilliams, 2016), where  $H$  is the mixed layer depth, and  $\nabla_h b$  is the horizontal buoyancy gradient at the front.

During SI, restratification occurs primarily via a horizontal buoyancy flux associated with the vertically-sheared cross-front flow (Taylor and Ferrari, 2010). Bachman et al. (2017a) proposed a parameterization for restratification by SI. Since SI is generally faster than MLI, in an initial value problem (or following a sudden forcing event) SI typically acts in the early stages of the response before transitioning to MLI (Stamper and Taylor, 2017). In the idealized experiments of Fox-Kemper et al. (2008), SI brings the front to  $Ri = 1$ , i.e.,  $N^2 = |\nabla_h b|^2/f^2$ , then MLI becomes the primary instability process. The complementary roles of symmetric and MLI are illustrated by the simulations of frontal regions under destabilizing heat forcing in Taylor and Ferrari (2011): restratification occurs very rapidly (less than a day) due to SI whereas MLI achieves a much stronger restratification but on much longer times (several days). In Verma et al. (2019) as well, during the spindown of a front, the initial configuration with  $Ri = 0.26$  is unstable to SI that then develops secondary KH instability and three-dimensional turbulence. The MLI soon becomes the dominant mode as  $Ri$  increases to beyond 0.95 during restratification of the front.

Restratification driven by finite-amplitude MLI is an adiabatic process that can be represented through advection by an eddy-driven overturning streamfunction (Boccaletti et al., 2007; Fox-Kemper et al., 2008):

$$\Psi^* \sim -C_e \frac{H^2 |\nabla_h b|}{f} \quad (27)$$

and an associated buoyancy flux:

$$\overline{w'b'} \sim C_e \frac{H^2 |\nabla_h b|^2}{f}, \quad (28)$$

with  $C_e \approx 0.06$  determined from idealized experiments by Fox-Kemper et al. (2008). A parameterization of MLI restratification effects has been developed by Fox-Kemper et al. (2008); Fox-Kemper and Ferrari (2008) based on this scaling, analogously to what was done by Gent and Mcwilliams (1990) to parameterize interior baroclinic instability for non-eddying ocean models. This parameterization contributed to improve the properties of the mixed-layer in climate models (Fox-Kemper et al., 2011; Gent et al., 2011). For example, it can reduce the maximum mixed-layer depth by up to 200 m in the Southern Ocean and correct

systematic biases with important climatic impacts (Calvert et al., 2020). However it was also noted by Callies and Ferrari (2018b) that this scaling only represents  
 985 the initial phase of the instability, but is not valid anymore when MLI reaches the finite-amplitude stage and develop larger eddies and stronger velocities than assumed in the scalings. In the numerical experiments of Capet et al. (2008b), for example, the submesoscale vertical buoyancy flux due predominantly to MLI is  $\sim 100 \text{ W m}^{-2}$ , exceeding the prediction of Eq. 28. Note, however, that the rate  
 990 of restratification by MLI may be impacted by the parameterization of vertical eddy viscosity in a given model (Mukherjee et al., 2016).

### 0.3.2 Competition between destratification and restratification of a front

The two main factors driving turbulence in the mixed layer are the surface  
 995 buoyancy flux and wind. When the horizontal density gradient is sufficiently weak, surface cooling (corresponding to a surface buoyancy flux  $B_0 > 0$ ) will drive mixing and destratification through convection. Wind blowing over a front may restratify the mixed layer if the wind is blowing upfront (and advecting light water over dense water) or destratify if the wind is blowing downfront (and advecting dense water over light water). As discussed in subsection 0.2.2.3, the  
 1000 wind drives an Ekman buoyancy flux (EBF) that scales as:

$$\text{EBF} \sim \tau_w^a \frac{|\nabla_h b|}{\rho f}, \quad (29)$$

where  $\tau_w^a$  is the along-front wind stress. Note however that, even though the relative orientation of fronts and winds is nearly isotropic on a global scale, there  
 1005 is an asymmetry in the processes leading to a larger upwind restratification than downfront destratification for an equal wind stress (Thomas and Ferrari, 2008).

In the presence of wind forcing, the impact of the submesoscale processes on restratification can be different than the picture drawn in the previous sub-section. Depending on the relative strengths of the wind-driven Ekman flow and the frontal ASC, wind-driven destratification can overcome restratification  
 1010 induced by the ASC related to frontogenesis (Thomas and Ferrari, 2008). The competition between destratification by downfront winds and restratification by MLI has been studied by Mahadevan et al. (2010). The relative importance of the destratification by down-front winds compared to the restratification by MLI  
 1015 can be characterized by a ratio between the respective buoyancy fluxes. Using Eq. 29 and Eq. 28, this ratio is:

$$R = \frac{\tau_w^a}{C_e H^2 \rho |\nabla_h b|}. \quad (30)$$

In the simulations of Mahadevan et al. (2010), the ratio is equal to 1 and the restratification by MLI is countered by a down-front wind stress  $\tau_w \approx 0.2 \text{ N}$

1020  $\text{m}^{-1}$ . However, the amplitude of the destratifying buoyancy flux diminishes with time as the alignment between the wind and front is disrupted by the growth of the frontal instability.

1025 MLI is relatively resilient to convective mixing and found to grow in most conditions. MLI shuts off convection in conditions of weak buoyancy forcing (Mahadevan et al., 2010). MLI is also active and capable of generating submesoscale eddies in the presence of strong convection even if it is unable to completely restratify the flow and shut off convection (Callies and Ferrari, 2018a). The convective deepening of the mixed-layer is partially balanced by the submesoscale buoyancy flux due to MLI, leading to a more heterogeneous and shallower mixed-layer than would be the case in the absence of submesoscales (Couvelard et al., 2015). A similar resilience of MLI-driven restratification was observed during the passage of an intense idealized autumn storm by Whitt and Taylor (2017). Despite the strong destratifying effect due to downfront winds, the submesoscales intensified during the storm and maintained a strong stratification in local patches. Considering a balance between MLI and the effect of a fixed vertical diffusion would imply a restratification rate one order of magnitude larger than Eq. 28 (Bachman and Taylor, 2016). In a more realistic situation, based on a submesoscale-resolving simulation of the central part of the Baltic Sea, Chrysagi et al. (2021) confirmed that submesoscales are able to maintain shallow mixed-layer depths in local patches during the passage of storms and that a rapid restratification is at work after the passage of the storms. This submesoscale restratifying effect has important implications because the mixing efficiency can remain high ( $\Gamma = 0.2$ ) at submesoscale fronts, contrary to regions where the mixed-layer is already well-mixed (Chrysagi et al., 2021).

1045 Global estimates using Argo profiling float observations highlight the importance of MLI to the restratification of the upper ocean (Johnson et al., 2016). The mechanism is particularly effective in the regions and times where the mixed-layer is deep, in particular during the transition from winter to spring when the mixed-layer is at its deepest. Regions of deep convection (Haine and Marshall, 1999) and inside anticyclones (Bosse et al., 2019) are also characterized by 1050 enhanced MLI-driven restratification. A number of in-situ observations have confirmed the importance of the MLI-driven restratification around the globe: e.g., in the north-east Pacific (Hosegood et al., 2006), in the Southern ocean (Bachman et al., 2017b; du Plessis et al., 2017), or in the Antarctic Marginal Ice Zone and under sea ice, where the equivalent heat flux can reach  $\sim 240 \text{ W m}^{-2}$  in mid-winter (Biddle and Swart, 2020). However, the few high-resolution 1055 observations at individual fronts, like the ones taken along the rim of a Southern Ocean mesoscale eddy (Adams et al., 2017) or over a California Current upwelling front (Johnson et al., 2020a,b), are also exposing that the destratification/restratification of the front is often complex and involve interactions between many processes.

1060 Observations of submesoscale fronts over long periods are very difficult to

obtain, and the Ocean Surface Mixing, Ocean Submesoscale Interaction Study (OSMOSIS), which took place in the north-east Atlantic, is one rare example. 1065 The year-long records of in-situ measurements from a glider and a mooring array highlight a strong seasonal cycle of submesoscale turbulence (Buckingham et al., 2016) with several instabilities controlling the stratification of the upper ocean: The mixed-layer deepens in the fall due to GI, and is restratified by SI and MLI throughout the winter (Thompson et al., 2016; Yu et al., 2019b).

1070 Year-long observations were also obtained with a similar mooring array in the North Pacific Subtropical Counter-current during the SubMESI experiment (Zhang et al., 2020). The SubMESI mooring was located in a region more typical of subtropical gyres with a shallower mixed-layer and higher eddy kinetic energy than the north-east Atlantic. Submesoscale turbulence is driven there by a combination of MLI and strain-induced frontogenesis leading to an equivalent 1075 upward heat flux comparable in magnitude with the net surface heat fluxes during late winter and early spring.

1080 Submesoscale processes play an important role in the surface mixed-layer, but it remains unclear how effectively they can penetrate into the underlying pycnocline and significantly contribute to vertical heat and buoyancy fluxes in the interior. Intense frontogenetic regions with ageostrophic dynamics are present in the ocean interior in the idealized simulations of Molemaker et al. 1085 (2010) and Barkan et al. (2015). However, the dynamical regimes in these simulations are characterized by a large  $M^2/N^2$  ratio (= 0.2 in Molemaker et al. (2010)) compared to typical interior ocean values (see discussion in Capet et al. (2016)).

1090 Examples of submesoscale fronts that penetrate below the mixed layer have been documented by Yu et al. (2019a); Zhang et al. (2020). Recent observations and modelling in the Southern Ocean have highlighted the presence of deep 1095 submesoscale fronts reaching down to 1000 m depth. These fronts are generated by the straining associated with Southern ocean mesoscale eddies and are associated with active frontogenesis. They drive an anomalous upward heat transport from the ocean interior to the surface that acts to restratify the ocean interior (Siegelman et al., 2020; Siegelman, 2020). Similar deep reaching fronts might be present in regions with strong horizontal gradients (*e.g.*, western boundary currents and regions with intense mesoscale activity) and low stratification (*e.g.*, high latitudes regions). The submesoscale vertical heat transport computed at 200 m depth by Su et al. (2018, their Fig. 3c,d) might give a good idea of where to expect such deep reaching fronts.

### 0.3.3 Bottom boundary layer mixing and restratification

1100 In the BBL, unbalanced submesoscale processes linked to negative PV (GI, CI, SI) can produce small-scale turbulence and contribute to mixing the fluid toward a state of marginal stability. Recent observations by Ruan et al. (2017) in the southern Drake Passage have highlighted the presence of strong lateral buoy-

1105  
 ancy gradients along slopes and enhanced bottom turbulence associated with submesoscale instabilities, leading to thick bottom mixed layers and water-mass modifications. Observations in the Orkney passage, shown in Fig. 12, have also highlighted a vigorous turbulent mixing associated with submesoscale instabilities, in particular CI and SI (Naveira Garabato et al., 2019). Microstructure measurements led to turbulent dissipation and mixing rates exceeding oceanic background values by one to three orders of magnitude in the abyssal boundary current. However, to maintain efficient water-mass transformations, it is also essential that the mixed waters are exported out of the mixed-layer and replaced by stratified waters from the interior. These instabilities also drive such lateral exchanges (Naveira Garabato et al., 2019), leading to a high mixing efficiency 1110  
 1115 (0.6 - 1) compared to a typical efficiency of 0.2 (Springy et al., 2021).

The contribution of topographic wakes to mixing may also be significant as the mixing efficiency of CI is particularly high in the stratified interior (Dewar et al., 2015; Jiao and Dewar, 2015; Gula et al., 2016). In the idealized numerical experiments of Perfect et al. (2020), large volume-averaged diapycnal diffusivities are found in the wake of a seamount. They are shown to scale like the product of the Froude and Rossby numbers squared :  $K_{rho} \sim (Fr Ro)^2 = (\frac{U}{NH} \frac{U}{fD})^2$ , where  $H$  and  $D$  are the height and full width at half maximum of the seamount.

1120  
 1125 Similarly to the surface, bottom MLI draws energy through the vertical buoyancy flux and contributes to a restratification of the bottom mixed layer ( $w'b' > 0$ ). MLI is thus suspected to directly affect the strength and structure of the abyssal overturning circulation by playing a crucial role to balance the effect of bottom-intensified mixing and allow for sustained water mass transformations (Callies, 2018), see also chapter 3 and 7. The stratification over the flanks of mid-ocean ridge systems seem to be largely maintained by submesoscale baroclinic eddies, contrary to the stratification within ridge-flank canyons, which 1130  
 1135 is maintained by mixing-driven mean flows (Ruan and Callies, 2020).

#### 0.4 REDISTRIBUTION OF PASSIVE TRACERS AND PARTICLES

In this section, we describe the role of submesoscale processes in redistributing 1135  
 1140 passive ocean tracers (those that do not affect the density of sea water). We consider two kinds of passive tracers: Firstly, those that are *conservative*, i.e. have no interior sources and sinks, and hence affected only by boundary fluxes, physical transport, and mixing. Secondly, those that are *reactive*, i.e. altered by growth and decay processes. Naturally most biogeochemical tracers are regarded as reactive, since they are affected by biological growth or decay that occurs in the presence of another variable or property, such as photosynthesis in the sunlit region.

The same tracers may exhibit different active/passive or conservative/reactive behaviors depending on the situation. For example, temperature and salinity affect the density of sea water and therefore are undeniably active. However, 1145  
 1150 most currents in the ocean are isopycnal, even at the submesoscales. When

such motions are considered, temperature or salinity anomalies act as *passive* tracers that are stirred on isopycnal surfaces by the eddying flow field. Density-compensated thermohaline variability is often the most convenient passive tracer to study, since it is found ubiquitously in the world's oceans even where other passive tracers may be absent.

Discrete particulate matter suspended in the ocean (such as plankton, larvae, sediment, microplastics, oil droplets, etc.) as well as macroscopic objects (marine debris, kelp, ice floes) often behave similarly to passive tracers, although their redistribution is additionally complicated by the buoyancy and inertia effects.

#### 0.4.1 Conservative tracers

Conservative passive tracers in the ocean are stirred by the eddying flow field, creating tracer variability over a range of scales. This variability can be characterized by an isopycnal spectrum of a tracer variance  $P(k)$ , where  $k$  is the horizontal wave number. The passive tracer spectrum is theoretically predicted to be universally related to the stirring eddy flow field and its turbulent kinetic energy spectrum  $E(k)$ , at least for well developed turbulence (Vallis, 2006): For a uniformly rolling-off kinetic energy spectrum  $E(k) \sim k^{-n}$ ,  $n < 3$ , the corresponding conservative passive tracer variance spectrum rolls off as

$$P(k) \sim k^{(n-5)/2}. \quad (31)$$

In the interior ocean, quasi-geostrophic dynamics suggests that  $E(k) \sim k^{-3}$ , corresponding to the tracer variance spectrum  $P(k) \sim k^{-1}$ . On the other hand, surface-quasigeostrophic theory applicable to near-surface submesoscale processes produces kinetic energy and passive tracer spectra with the same slope, *i.e.*,  $E(k) \sim P(k) \sim k^{-5/3}$ . Relationship (31) breaks down for steep kinetic energy spectra ( $n > 3$ ), where stirring becomes non-local and  $P(k) \sim k^{-1}$  (Batchelor, 1959). As (31) suggests, when smaller scale turbulence is more energetic (the  $E(k)$  spectrum is flatter) there is more vigorous stirring of passive tracers, resulting in less tracer variance at smaller scales and a steeper tracer variance spectrum,  $P(k)$  (Scott, 2006; Callies and Ferrari, 2013; Jaeger et al., 2020a).

A number of observational studies have tried to analyze the spectra of passive tracers in the pycnocline, but until recently, they lacked the horizontal resolution to conclusively measure the spectrum at submesoscales. A major oceanographic field experiment called LatMix (Scalable Lateral Mixing and Coherent Turbulence, Shcherbina et al., 2015), aimed at observing submesoscale stirring, was conducted in 2012 in the northwestern Atlantic. Direct measurements of dye dispersion highlighted stirring by submesoscale eddies (Sundermeyer et al., 2014). Spectra of salinity anomalies along isopycnals, which behave mostly like a passive tracer, pointed to a steeper variance at submesoscale than expected from (surface) quasi-geostrophic motions (Kunze et al., 2015), consistent with

other sets of observations (Klymak et al., 2015). Another recent study (Jaeger et al., 2020b) that compiled 4,800 km of ship track with underway-CTD profiles at spacings of 0.3–3 km in the Bay of Bengal, also showed a steepening of the tracer variance spectrum at submesoscales, suggesting that submesoscales are acting to mix tracers along isopycnal surfaces in the pycnocline. Submesoscale streamers were also observed during the LatMix experiment which were associated with a significant freshwater flux across the sharp north wall of the Gulf Stream (Klymak et al., 2016), which was previously considered as a barrier to lateral mixing. These exchanges across the Gulf Stream front have been further characterised using dye observations and numerical simulations as a result of a combination of strong vertical mixing events and shear dispersion induced by submesoscale instabilities (Wenegrat et al., 2020).

Submesoscale isopycnal stirring appears to vary strongly across isopycnals, creating complex vertical interleaving of water masses (Shcherbina et al., 2009; Jaeger et al., 2020a). Interleaving layers can be 1–10 m thick, tens of kilometers in horizontal extent, and tends to be tilted with respect to the isopycnals. These interleaving intrusions of water are generated by the swirling flow associated with eddies, both at mesoscales (Smith and Ferrari, 2009) and submesoscales. The submesoscale signatures suggest that the vertical shear of the horizontal velocity, which is associated with the strong lateral density gradients in the mixed layer, is critical for generating layers in water mass anomaly that are tilted with respect to the isopycnal surfaces (Jaeger et al., 2020a). The very thin (depth to length) aspect ratio of the layers creates a strong vertical gradient in the tracers, which is then smoothed through diapycnal mixing. In this way, lateral stirring by submesoscale processes creates thin layers with sharp vertical gradients that result in enhanced diapycnal mixing.

#### 0.4.2 Mixing and transport of reactive tracers

Along-isopycnal vertical transport is associated with isopycnal stirring, which becomes more efficient with submesoscale dynamics. This is why submesoscale processes are responsible for enhancing the vertical transport of biogeochemical tracers such as nutrients, carbon and oxygen (Thomas et al., 2008). The net vertical flux of a biogeochemical tracer is the integral of  $w c'$ , where  $c'$  is the tracer anomaly from the tracer mean at that depth. Hence, the flux depends on the covariance of the vertical velocity and tracer anomaly, and is dependent on the relative timescales for the biogeochemical reaction (or modification) and vertical transport. This is one of the reasons that submesoscale vertical velocities are efficient in transporting biogeochemical properties (Whitt et al., 2019).

Model simulations have shown that increasing horizontal grid resolution leads to a greater vertical supply of nutrients (Lévy et al., 2012; Uchida et al., 2020) and stronger tracer subduction into the pycnocline (Balwada et al., 2018). A careful analysis (Freilich and Mahadevan, 2019) shows that although the

1230 vertical uplift of isopycnals is the larger component of vertical transport, the along-isopycnal component of vertical transport is more sensitive to model resolution and accounts for a larger fraction of vertical flux when the submesoscale activity is increased.

#### 0.4.3 Impacts on the dispersion of buoyant material

1235 Surface submesoscale currents can produce strong local dispersion (spreading) of passive tracers down to 100 m scales with implications for the predictive modeling of oceanic pollutants (Poje et al., 2014). At the same time, frontogenetic submesoscale flows are characterized by zones of sharp convergences of horizontal currents at the ocean surface (see discussion in Section 0.2.1), which are naturally anti-dispersive. Convergence zones concentrate buoyant material, such 1240 as plankton, natural surfactants, pollutants (particularly, oil and oil degradation products), and marine debris. Highly buoyant material remains close to the surface, therefore breaking the three-dimensional non-divergence, and allowing strong accumulation within convergence zones (D'Asaro et al., 2018).

1245 Taylor (2018) used large-eddy simulations of MLI under various intensities of convective forcing to study the influence of submesoscales on buoyant tracers. When the buoyant rise velocity was not small compared to the *rms* vertical fluid velocity, the buoyancy tracers accumulate near the surface in a submesoscale front that wraps around the submesoscale eddy, mirroring the patterns seen in observations (D'Asaro et al., 2018). Intense downwelling at the submesoscale 1250 front pulls the buoyant tracers beneath the surface. In some cases this results in the buoyant tracer extending deeper into the water column than it would in the absence of submesoscales.

#### 0.4.4 Dispersion by the deep submesoscale currents

1255 Submesoscale currents also contribute to the dispersion and transport of passive tracers at the bottom and in the interior of the ocean. Submesoscale currents (as well as tidal currents) generate significant horizontal and vertical dispersion of tracers close to the topography. For example, over the Mid-Atlantic ridge, submesoscale currents have been shown to influence dispersion of deep-sea hydrothermal vents effluents and larvae and impact connectivity between deep-sea ecosystems (Vic et al., 2018).

1260 Deep submesoscale currents can also generate long-range anomalous transport of tracers in the ocean interior in the form of subsurface submesoscale eddies, known as Submesoscale Coherent Vortices (SCVs) (McWilliams, 1985) or Intra Thermocline Eddies (ITEs) (Dugan et al., 1982). SCVs are usually defined as energetic eddies with a radius smaller than the Rossby deformation radius, a structure localized in the vertical, and an interior velocity maximum (McWilliams, 1985). SCVs may be generated due to various frictional or di-

abatic effects, which include: convection (Marshall and Schott, 1999), wind-driven destruction of PV (Thomas, 2008), geothermal forcing (Baker et al., 1270 1987), bottom mixing (McWilliams, 1985), or friction (D'Asaro, 1988), or by inviscid instability processes of bottom currents such as baroclinic instability (Morvan et al., 2019). Topographic wakes are suspected to be the major source of SCVs (McWilliams, 2016).

SCVs can be very long-lived ( $> 1$  year) and travel far from their origins, 1275 being primarily advected by mesoscale and mean currents. One of the most well-known types of SCVs are Meddies (even if they are formally closer to mesoscale than submesoscale) formed at the exit of the Mediterranean Sea (McDowell and Rossby, 1978), which spread salty Mediterranean waters in the subtropical Atlantic ocean. SCVs that form in eastern boundary regions are 1280 essential for spreading oxygen-poor and nutrient-rich waters into the interior of gyres (Frenger et al., 2018). SCVs also form from wintertime deep convection, as observed in the Labrador Sea (Clarke, 1984; Lilly and Rhines, 2002) and the northwestern Mediterranean Sea (Testor and Gascard, 2003; Bosse et al., 2016, 1285 2017) where they are essential for spreading the newly formed deep waters within ocean basins. SCVs formed in the wake of topographic features, for example the Charleston Bump along the U.S. seaboard, can transport waters from the bottom mixed layer over long distances and spread them within the subtropical gyre (Gula et al., 2019).

SCVs have always been very difficult to sample due to the sparsity of in situ 1290 observations able to resolve submesoscales in the interior of the ocean. Thanks to the coverage of Argo floats, it is now possible to make more robust statistics on the existence and properties of the SCVs (Li et al., 2017; McCoy et al., 2020). The cumulative effect of SCVs could potentially affect the large-scale transport 1295 and distribution of heat, nutrients, and biogeochemical tracers. However, a quantitative assessment of such impacts still remain to be done.

## 0.5 CONCLUSION AND FUTURE DIRECTIONS

As an intermediary between balanced flows and small-scale turbulence, submesoscales play an important part in the story of ocean mixing. Through the instabilities described in sections 0.2.2 and 0.2.3, submesoscales restratify the 1300 surface and bottom mixed layers (see section 0.3), while turbulent mixing influences the evolution of submesoscale fronts by generating a cross-front circulation as described in section 0.2.4. At the same time, submesoscales drive strong vertical circulations that re-distribute passive, active, reactive, and buoyant tracers while stirring tracers along isopycnals, transporting material through the ocean 1305 interior and shortening the route to small-scale mixing (section 0.4).

The body of knowledge on submesoscale processes has grown substantially over the last 15 years. However, many theoretical and modelling studies have considered only a subset of the submesoscale processes mentioned here – either by design or by limitations in resolution. The multi-scale interactions between

1310 various processes (*e.g.*, boundary layer turbulence, SI, MLI, internal waves, and mesoscale eddies) remains relatively unexplored. Recent advances in computational power have made it possible to begin to study at least some of these interactions. For example, Skillingstad and Samelson (2020) used large-eddy simulations to study the interaction between boundary layer turbulence, SI, and  
 1315 MLI, while submesoscale-permitting global ocean models (*e.g.*, Su et al., 2018, 2020) have provided insight into the influence of submesoscales on large-scale circulation and heat transport. Piecing together the links between small-scale turbulence and mixing, submesoscales, mesoscale eddies, internal waves and the general circulation remains a grand challenge.

1320 The effect of air-sea coupling at the submesoscale on the ocean surface layer is also relatively unexplored. Using submesoscale-resolving numerical simulations, Renault et al. (2018) found a sink of energy at the submesoscale related to induced Ekman pumping velocities, but also an increase of the injection of energy by baroclinic conversion into the submesoscale. The effect of waves  
 1325 and Langmuir turbulence on the submesoscale processes described above is also a relatively new topic. Some studies have shown that Langmuir turbulence can significantly increase small-scale turbulence and counter the restratifying effects of MLI (Hamlington et al., 2014), and that surface waves also have an impact on frontogenesis (Suzuki et al., 2016; Sullivan and McWilliams, 2019). A next step  
 1330 in our understanding of the oceanic submesoscale processes and their impact on the stratification of the ocean surface layer may require a fully interactive atmosphere as well as the wave feedbacks, which will modulate the turbulent exchanges of momentum, heat and tracers between the atmosphere and ocean.

1335 Submesoscale currents impact the large-scale ocean circulation in many counter-intuitive ways, including upscale energy transfer to mesoscale eddies or upgradient fluxes of tracers (Klein et al., 2019). Recent studies are highlighting the global impacts of submesoscales, for example the contribution of near-surface submesoscale currents in driving vertical heat fluxes (Su et al., 2018, 2020) and restratifying the upper ocean (Johnson et al., 2016). The role played  
 1340 by submesoscale instabilities at the bottom, which has been discovered much more recently, may also be a very important ingredient for the generation of near bottom mixing, the export of buoyancy and ultimately for the closure of the overturning circulation.

1345 Unfortunately the current generation of OGCM is far from being able to resolve the full range of submesoscale processes in the surface and bottom boundary layers. In the ongoing CMIP6 exercise, ocean models will typically have a 1/4 degree resolution, allowing for mesoscales but not totally resolving them (Griffies et al., 2016). One can expect that truly mesoscale-resolving ocean models will be a standard for climate studies a decade from now, but the use of  
 1350 submesoscale-resolving models in climate studies might still be several decades away – up to 40-50 years based on Moore’s law (Dong et al., 2020b). More precisely, according to the global estimates of Dong et al. (2020b) and Dong et al. (2021) (see Fig. 6), the required grid spacing to resolve MLI over 90 % of

the ocean's surface is about 1 km in winter and 500 m in summer, for BMLI it falls to about 100 m, and finally less than 10 m for SI. The current state-of-the-art for global or basin-scale forced ocean simulations have grid spacings on the order of 1-2 km (LLC4320 at 1/48°, eNATL60 at 1/60°, or GIGATL1 at 1 km), which can only be said to safely resolve winter MLI. Thus, these state-of-the-art models just scratch the surface of the submesoscale realm.

While submesoscales are not fully resolved in many models, many submesoscale effects on mixing have yet to be parameterized. Some parameterizations are already used in ocean models to incorporate the restratifying effects of MLI (Fox-Kemper et al., 2011; Calvert et al., 2020) and the extraction of energy from the geostrophic currents and diffusive tracer mixing due to SI and associated secondary shear instabilities (Bachman et al., 2017a; Dong et al., 2020c). These efforts are encouraging but these parameterizations still have issues (Calvert et al., 2020) and do not account yet for all the effects of submesoscales in the surface boundary layer. Furthermore, no parameterizations exist yet for bottom boundary submesoscale processes, and given their potential impact on the large-scale circulation, designing one should stand out as an important objective. The nonlinear, interacting processes active at the submesoscale makes the parameterization problem particularly challenging. However, recent developments in empirical data-driven methods and machine learning offer a promising path forward.

## ACKNOWLEDGEMENTS

The authors thanks C. Vic, J. Dong, B. Fox-Kemper, X. Yu, J. Wenegrat, and A. Naveira Garabato for providing the original data used to plot Figures 3,6,9,11,12. J. Gula gratefully acknowledges support from the French National Agency for Research (ANR) through the projects DEEPER (ANR-19-CE01-0002-01) and ISblue “Interdisciplinary graduate school for the blue planet” (ANR-17-EURE-0015).

## BIBLIOGRAPHY

- Adams, K. A., Hosegood, P., Taylor, J. R., Sallée, J.-B., Bachman, S., Torres, R., and Stamper, M. (2017). Frontal circulation and submesoscale variability during the formation of a southern ocean mesoscale eddy. *Journal of Physical Oceanography*, 47(7):1737–1753.
- Ajaii, A., Le Sommer, J., Chassignet, E. P., Molines, J.-M., Xu, X., Albert, A., and Dewar, W. (2021). Diagnosing cross-scale kinetic energy exchanges from two submesoscale permitting ocean models. *Journal of Advances in Modeling Earth Systems*, n/a(n/a):e2019MS001923. e2019MS001923 2019MS001923.
- Allen, J. S. and Newberger, P. A. (1998). On Symmetric Instabilities in Oceanic Bottom Boundary Layers. *Journal of Physical Oceanography*, 28(6):1131–1151.
- Bachman, S., Fox-Kemper, B., Taylor, J., and Thomas, L. (2017a). Parameterization of frontal symmetric instabilities. I: Theory for resolved fronts. *Ocean Modelling*, 109:72 – 95.
- Bachman, S. D. and Klocker, A. (01 Oct. 2020). Interaction of jets and submesoscale dynamics

- leads to rapid ocean ventilation. *Journal of Physical Oceanography*, 50(10):2873 – 2883.
- Bachman, S. D. and Taylor, J. R. (2016). Numerical Simulations of the Equilibrium between Eddy-Induced Restratiification and Vertical Mixing. *Journal of Physical Oceanography*, 46(3):919–935.
- Bachman, S. D., Taylor, J. R., Adams, K. A., and Hosegood, P. J. (2017b). Mesoscale and Submesoscale Effects on Mixed Layer Depth in the Southern Ocean. *Journal of Physical Oceanography*, 47(9):2173–2188.
- Baker, E. T., Massoth, G. J., and Feely, R. A. (1987). Cataclysmic hydrothermal venting on the Juan de Fuca Ridge. *Nature*, 329:149 EP –.
- Balwada, D., Smith, K. S., and Abernathey, R. (2018). Submesoscale vertical velocities enhance tracer subduction in an idealized antarctic circumpolar current. *Geophysical Research Letters*, 45(18):9790–9802.
- Barkan, R., Molemaker, M. J., Srinivasan, K., McWilliams, J. C., and D'Asaro, E. A. (2019). The role of horizontal divergence in submesoscale frontogenesis. *Journal of Physical Oceanography*, 49(6):1593–1618.
- Barkan, R., Winters, K. B., and Llewellyn Smith, S. G. (2015). Energy cascades and loss of balance in a reentrant channel forced by wind stress and buoyancy fluxes. *Journal of Physical Oceanography*, 45(1):272–293.
- Barth, J. (1989a). Stability of a coastal upwelling front, 1. Model development and a stability theorem. *J. Geophys. Res.*, 94:10844–10856.
- Barth, J. (1989b). Stability of a coastal upwelling front, 2. Model results and comparison with observations. *J. Geophys. Res.*, 94:10857–10883.
- Barth, J. (1994). Short-wavelength instabilities on coastal jets and fronts. *J. Geophys. Res.*, 99:16095–16115.
- Batchelor, G. K. (1959). Small-scale variation of convected quantities like temperature in turbulent fluid part 1. general discussion and the case of small conductivity. *Journal of Fluid Mechanics*, 5(1):113–133.
- Benthuyzen, J. and Thomas, L. (2012). Friction and diapycnal mixing at a slope: Boundary control of potential vorticity. *J. Phys. Oceanogr.*, 42:1509–1523.
- Biddle, L. C. and Swart, S. (2020). The observed seasonal cycle of submesoscale processes in the antarctic marginal ice zone. *Journal of Geophysical Research: Oceans*, n/a(n/a):e2019JC015587. e2019JC015587 2019JC015587.
- Blumsack, S. L. and Giersch, P. J. (1972). Mars: The effects of topography on baroclinic instability. *Journal of Atmospheric Sciences*, 29(6):1081 – 1089.
- Boccaletti, G., Ferrari, R., and Fox-Kemper, B. (2007). Mixed layer instabilities and restratification. *J. Phys. Oceanogr.*, 37:2228–2250.
- Bodner, A. S., Fox-Kemper, B., Van Roekel, L. P., McWilliams, J. C., and Sullivan, P. P. (2019). A perturbation approach to understanding the effects of turbulence on frontogenesis. *Journal of Fluid Mechanics*, 883:A25.
- Bosse, A., Fer, I., Lilly, J. M., and Søiland, H. (2019). Dynamical controls on the longevity of a non-linear vortex : The case of the lofoten basin eddy. *Scientific Reports*, 9(1):13448.
- Bosse, A., Testor, P., Houpert, L., Damien, P., Prieur, L., Hayes, D., Taillandier, V., Durrieu de Madron, X., d'Ortenzio, F., Coppola, L., Karstensen, J., and Mortier, L. (2016). Scales and dynamics of submesoscale coherent vortices formed by deep convection in the northwestern Mediterranean Sea. *J. Geophys. Res. Oceans*, 121(10):7716–7742.
- Bosse, A., Testor, P., Mayot, N., Prieur, L., D'Ortenzio, F., Mortier, L., Goff, H. L., Gourcuff, C., Coppola, L., Lavigne, H., and Raimbault, P. (2017). A submesoscale coherent vortex in the Ligurian Sea: From dynamical barriers to biological implications. *J. Geophys. Res. Oceans*, 122(8):6196–6217.

- Brannigan, L., Marshall, D. P., Naveira-Garabato, A., and Nurser], A. G. (2015). The seasonal cycle of submesoscale flows. *Ocean Modelling*, 92:69 – 84.
- 1445 Brink, K. (2013). Instability of a tidal mixing front in the presence of realistic tides and mixing. *Journal of Marine Research*, 71(3):227–251.
- Brink, K. H. (2012). Baroclinic instability of an idealized tidal mixing front. *Journal of Marine Research*, 70(4):661–688.
- 1450 Brink, K. H. (2016). Continental shelf baroclinic instability. part i: Relaxation from upwelling or downwelling. *Journal of Physical Oceanography*, 46(2):551 – 568.
- Brüggemann, N. and Eden, C. (2015). Routes to dissipation under different dynamical conditions. *Journal of Physical Oceanography*, 45(8):2149 – 2168.
- Buckingham, C. E., Gula, J., and Carton, X. (2021a). The role of curvature in modifying frontal instabilities. part i: Review of theory and presentation of a nondimensional instability criterion. *Journal of Physical Oceanography*, 51(2):299 – 315.
- 1455 Buckingham, C. E., Gula, J., and Carton, X. (2021b). The role of curvature in modifying frontal instabilities. part ii: Application of the criterion to curved density fronts at low richardson numbers. *Journal of Physical Oceanography*, 51(2):317 – 341.
- Buckingham, C. E., Lucas, N. S., Belcher, S. E., Rippeth, T. P., Grant, A. L. M., Le Sommer, J., Ajayi, A. O., and Naveira Garabato, A. C. (2019). The contribution of surface and submesoscale processes to turbulence in the open ocean surface boundary layer. *Journal of Advances in Modeling Earth Systems*, 11(12):4066–4094.
- Buckingham, C. E., Naveira Garabato, A. C., Thompson, A. F., Brannigan, L., Lazar, A., Marshall, D. P., George Nurser, A. J., Damerell, G., Heywood, K. J., and Belcher, S. E. (2016). Seasonality of submesoscale flows in the ocean surface boundary layer. *Geophysical Research Letters*, pages n/a–n/a. 2016GL068009.
- Callies, J. (2018). Restratiification of abyssal mixing layers by submesoscale baroclinic eddies. *Journal of Physical Oceanography*, 48(9):1995–2010.
- 1470 Callies, J. and Ferrari, R. (2013). Interpreting energy and tracer spectra of upper-ocean turbulence in the submesoscale range (1-200 km). *J. Phys. Oceanogr.*, 43:2456–2575.
- Callies, J. and Ferrari, R. (2018a). Baroclinic instability in the presence of convection. *Journal of Physical Oceanography*, 48(1):45–60.
- Callies, J. and Ferrari, R. (2018b). Note on the rate of restratiification in the baroclinic spindown of fronts. *Journal of Physical Oceanography*, 48(7):1543–1553.
- 1475 Callies, J., Ferrari, R., Klymak, J., and Gula, J. (2015). Seasonality in submesoscale turbulence. *Nat. Commun.*, 6:6862.
- Callies, J., Flierl, G., Ferrari, R., and Fox-Kemper, B. (2016). The role of mixed-layer instabilities in submesoscale turbulence. *Journal of Fluid Mechanics*, 788:5–41.
- Calvert, D., Nurser, G., Bell, M. J., and Fox-Kemper, B. (2020). The impact of a parameterisation of submesoscale mixed layer eddies on mixed layer depths in the nemo ocean model. *Ocean Modelling*, 154:101678.
- 1480 Capet, X., Campos, E. J., and Paiva, A. M. (2008a). Submesoscale activity over the argentinian shelf. *Geophysical Research Letters*, 35(15).
- Capet, X., McWilliams, J. C., Molemaker, M., and Shchepetkin, A. (2008b). Mesoscale to submesoscale transition in the California Current System. Part I: Flow structure, eddy flux, and observational tests. *J. Phys. Oceanogr.*, 38:29–43.
- 1485 Capet, X., McWilliams, J. C., Molemaker, M., and Shchepetkin, A. (2008c). Mesoscale to submesoscale transition in the California Current System. Part II: Frontal processes. *J. Phys. Oceanogr.*, 38:44–64.
- Capet, X., McWilliams, J. C., Molemaker, M. J., and Shchepetkin, A. F. (2008d). Mesoscale to

- submesoscale transition in the California current system. part iii: Energy balance and flux. *Journal of Physical Oceanography*, 38(10):2256–2269.
- Capet, X., Roullet, G., Klein, P., and Maze, G. (2016). Intensification of Upper-Ocean Submesoscale Turbulence through Charney Baroclinic Instability. *Journal of Physical Oceanography*, 46(11):3365–3384.
- Carpenter, J. R., Rodrigues, A., Schultze, L. K. P., Merckelbach, L. M., Suzuki, N., Baschek, B., and Umlauf, L. (2020). Shear instability and turbulence within a submesoscale front following a storm. *Geophysical Research Letters*, 47(23):e2020GL090365. e2020GL090365 10.1029/2020GL090365.
- Charney, J. G. (1973). *Planetary Fluid Dynamics*, chapter Symmetric Circulations in Idealized Models, pages 128–141. D. Reidel Publishing Company.
- Chelton, D. B., deSzoeke, R. A., Schlax, M. G., El Naggar, K., and Siwartz, N. (1998). Geographical variability of the first baroclinic Rossby radius of deformation. *Journal of Physical Oceanography*, 28(3):433–460.
- Chen, S.-N., Chen, C.-J., and Lerczak, J. A. (2020). On baroclinic instability over continental shelves: Testing the utility of Eady-type models. *Journal of Physical Oceanography*, 50(1):3 – 33.
- Chrysagi, E., Umlauf, L., Holtermann, P., Klingbeil, K., and Burchard, H. (2021). High-resolution simulations of submesoscale processes in the Baltic Sea: The role of storm events. *Journal of Geophysical Research: Oceans*, n/a(n/a):e2020JC016411. e2020JC016411 2020JC016411.
- Clarke, R. (1984). Transport through the Cape Farewell-Flemish Cap section. *Rapports et procès-verbaux des réunions - Conseil international pour l'exploration de la mer*, 185:120–130.
- Couvelard, X., Dumas, F., Garnier, V., Ponte, A., Talandier, C., and Treguier, A. (2015). Mixed layer formation and restratification in presence of mesoscale and submesoscale turbulence. *Ocean Modelling*, 96:243 – 253.
- Cronin, M. F. and Kessler, W. S. (2009). Near-surface shear flow in the tropical Pacific cold tongue front. *Journal of Physical Oceanography*, 39(5):1200–1215.
- Crowe, M. and Taylor, J. (2020). The effects of surface wind stress and buoyancy flux on the evolution of a front in a turbulent thermal wind balance. *Fluids*, 5(2):87.
- Crowe, M. N. and Taylor, J. R. (2018). The evolution of a front in turbulent thermal wind balance. part 1. theory. *Journal of Fluid Mechanics*, 850:179–211.
- Crowe, M. N. and Taylor, J. R. (2019). The evolution of a front in turbulent thermal wind balance. part 2. numerical simulations. *Journal of Fluid Mechanics*, 880:326–352.
- Cushman-Roisin, B. and Beckers, J.-M. (2011). *Introduction to geophysical fluid dynamics: physical and numerical aspects*. Academic press.
- D’Asaro, E. (1988). Generation of submesoscale vortices: A new mechanism. *J. Geophys. Res.*, 93(C6):6685–6693.
- D’Asaro, E., Lee, C., Rainville, L., Harcourt, R., and Thomas, L. (2011). Enhanced turbulence and energy dissipation at ocean fronts. *Science*, 332(318).
- D’Asaro, E. A., Carlson, D. F., Chamecki, M., Harcourt, R. R., Haus, B. K., Fox-Kemper, B., Molemaker, M. J., Poje, A. C., and Yang, D. (2020). Advances in observing and understanding small-scale open ocean circulation during the Gulf of Mexico Research Initiative era. *Frontiers in Marine Science*, 7:349.
- D’Asaro, E. A., Shcherbina, A. Y., Klymak, J. M., Molemaker, J., Novelli, G., Guigand, C. M., Haza, A. C., Haus, B. K., Ryan, E. H., Jacobs, G. A., Huntley, H. S., Laxague, N. J. M., Chen, S., Judt, F., McWilliams, J. C., Barkan, R., Kirwan, A. D., Poje, A. C., and Özgökmen, T. M. (2018). Ocean convergence and the dispersion of flotsam. *Proceedings of the National Academy of Sciences*, 115(6):1162–1167.

- 1540 Dauhajre, D. P. and McWilliams, J. C. (2018). Diurnal evolution of submesoscale front and filament circulations. *Journal of Physical Oceanography*, 48(10):2343–2361.
- Dauhajre, D. P., McWilliams, J. C., and Uchiyama, Y. (2017). Submesoscale coherent structures on the continental shelf. *Journal of Physical Oceanography*, 47(12):2949 – 2976.
- Dewan, W., Molemaker, M., and McWilliams, J. C. (2015). Centrifugal instability and mixing in the California Undercurrent. *J. Phys. Oceanogr.*, 45:1224–1241.
- 1545 Dong, J., Fox-Kemper, B., Zhang, H., and Dong, C. (2020a). The seasonality of submesoscale energy production, content, and cascade. *Geophysical Research Letters*, 47(6):e2020GL087388. e2020GL087388 2020GL087388.
- Dong, J., Fox-Kemper, B., Zhang, H., and Dong, C. (2020b). The scale of submesoscale baroclinic instability globally. *Journal of Physical Oceanography*.
- 1550 Dong, J., Fox-Kemper, B., Zhang, H., and Dong, C. (2021). The scale and activity of symmetric instability globally. *Journal of Physical Oceanography*.
- Dong, J., Fox-Kemper, B., Zhu, J., and Dong, C. (2020c). Application of symmetric instability parameterization in the coastal and regional ocean community model (croco). *Earth and Space Science Open Archive*, page 30.
- 1555 du Plessis, M., Swart, S., Ansorge, I. J., and Mahadevan, A. (2017). Submesoscale processes promote seasonal restratification in the subantarctic ocean. *Journal of Geophysical Research: Oceans*, 122(4):2960–2975.
- Dugan, J. P., Mied, R. P., Mignerey, P. C., and Schuetz, A. F. (1982). Compact, intrathermocline eddies in the Sargasso Sea. *J. Geophys. Res. Oceans*, 87(C1):385–393.
- 1560 Durski, S. and Allen, J. (2005). Finite-amplitude evolution of instabilities associated with the coastal upwelling front. *J. Phys. Oceanogr.*, 35:1606–1628.
- Eady, E. (1949). Long waves and cyclone waves. *Tellus*, 1:33–52.
- Ekman, V. W. (1905). On the influence of the earth's rotation on ocean-currents.
- Eliassen, A. and Kleinschmidt, E. (1957). Dynamic meteorology. In *Geophysik II/Geophysics II*, pages 1–154. Springer.
- 1565 Fadeev, E., Wietz, M., von Appen, W.-J., Nöthig, E.-M., Engel, A., Grosse, J., Graeve, M., and Boetius, A. (2020). Submesoscale dynamics directly shape bacterioplankton community structure in space and time. *bioRxiv*.
- Ferrari, R. and Rudnick, D. L. (2000). Thermohaline variability in the upper ocean. *Journal of Geophysical Research: Oceans*, 105(C7):16857–16883.
- 1570 Fox-Kemper, B., Danabasoglu, G., Ferrari, R., Griffies, S., Hallberg, R., Holland, M., Maltrud, M., Peacock, S., and Samuels, B. (2011). Parameterization of mixed layer eddies. iii: Implementation and impact in global ocean climate simulations. *Ocean Modelling*, 39(1):61 – 78. Modelling and Understanding the Ocean Mesoscale and Submesoscale.
- Fox-Kemper, B. and Ferrari, R. (2008). Parameterization of mixed layer eddies. part ii: Prognosis and impact. *Journal of Physical Oceanography*, 38(6):1166–1179.
- Fox-Kemper, B., Ferrari, R., and Hallberg, R. (2008). Parameterization of mixed layer eddies. Part I: Theory and diagnosis. *J. Phys. Oceanogr.*, 38:1145–1165.
- Freilich, M. A. and Mahadevan, A. (2019). Decomposition of Vertical Velocity for Nutrient Transport in the Upper Ocean. *Journal of Physical Oceanography*, 49(6):1561–1575.
- 1580 Frenger, I., Bianchi, D., Stührenberg, C., Oschlies, A., Dunne, J., Deutsch, C., Galbraith, E., and Schütte, F. (2018). Biogeochemical role of subsurface coherent eddies in the ocean: Tracer cannonballs, hypoxic storms, and microbial stewpots? *Global Biogeochem. Cy.*, 32(2):226–249.
- Fu, L.-L. and Ferrari, R. (2008). Observing oceanic submesoscale processes from space. *Eos, Transactions American Geophysical Union*, 89(48):488–488.
- Garrett, C. and Loder, J. (1981). Dynamical aspects of shallow sea fronts. *Phil. Trans. R. Soc. Lond.*,

- 302:563–581.
- Gent, P. R., Danabasoglu, G., Donner, L. J., Holland, M. M., Hunke, E. C., Jayne, S. R., Lawrence, D. M., Neale, R. B., Rasch, P. J., Vertenstein, M., Worley, P. H., Yang, Z.-L., and Zhang, M. (2011). The Community Climate System Model Version 4. *Journal of Climate*, 24(19):4973–4991.
- Gent, P. R. and McWilliams, J. C. (1990). Isopycnal Mixing in Ocean Circulation Models. *Journal of Physical Oceanography*, 20(1):150–155.
- Griffies, S. M., Danabasoglu, G., Durack, P. J., Adcroft, A. J., Balaji, V., Böning, C. W., Chassignet, E. P., Curchitser, E., Deshayes, J., Drange, H., Fox-Kemper, B., Gleckler, P. J., Gregory, J. M., Haak, H., Hallberg, R. W., Heimbach, P., Hewitt, H. T., Holland, D. M., Ilyina, T., Jungclaus, J. H., Komuro, Y., Krasting, J. P., Large, W. G., Marsland, S. J., Masina, S., McDougall, T. J., Nurser, A. J. G., Orr, J. C., Pirani, A., Qiao, F., Stouffer, R. J., Taylor, K. E., Treguier, A. M., Tsujino, H., Uotila, P., Valdivieso, M., Wang, Q., Winton, M., and Yeager, S. G. (2016). Omip contribution to cmip6: experimental and diagnostic protocol for the physical component of the ocean model intercomparison project. *Geoscientific Model Development*, 9(9):3231–3296.
- Gula, J., Blacic, T. M., and Todd, R. E. (2019). Submesoscale coherent vortices in the Gulf Stream. *Geophys. Res. Lett.*, 46.
- Gula, J., Molemaker, M., and McWilliams, J. C. (2014). Submesoscale cold filaments in the Gulf Stream. *J. Phys. Oceanogr.*, 44(10):2617–2643.
- Gula, J., Molemaker, M., and McWilliams, J. C. (2015a). Gulf Stream dynamics along the South-eastern U.S. Seaboard. *J. Phys. Oceanogr.*, 45(3):690–715.
- Gula, J., Molemaker, M., and McWilliams, J. C. (2015b). Topographic vorticity generation, submesoscale instability and vortex street formation in the Gulf Stream. *Geophys. Res. Lett.*, 42:4054–4062.
- Gula, J., Molemaker, M., and McWilliams, J. C. (2016). Topographic generation of submesoscale centrifugal instability and energy dissipation. *Nat. Commun.*, 7:12811.
- Haine, T. and Marshall, J. (1999). Gravitational, symmetric, and baroclinic instability of the ocean mixed layer. *J. Phys. Oceanogr.*, 28:634–658.
- Hamlington, P. E., Van Roekel, L. P., Fox-Kemper, B., Julien, K., and Chini, G. P. (2014). Langmuir–submesoscale interactions: Descriptive analysis of multiscale frontal spindown simulations. *Journal of Physical Oceanography*, 44(9):2249–2272.
- Hetland, R. D. (2017). Suppression of baroclinic instabilities in buoyancy-driven flow over sloping bathymetry. *Journal of Physical Oceanography*, 47(1):49–68.
- Hosegood, P., Gregg, M. C., and Alford, M. H. (2006). Sub-mesoscale lateral density structure in the oceanic surface mixed layer. *Geophysical Research Letters*, 33(22).
- Hoskins, B. J. (1974). The role of potential vorticity in symmetric stability and instability. *Q.J.R. Meteorol. Soc.*, 100:480–482.
- Hoskins, B. J. (1982). The mathematical theory of frontogenesis. *Ann. Rev. Fluid Mech.*, 14:131–151.
- Hoskins, B. J. and Bretherton, F. P. (1972). Atmospheric frontogenesis models: mathematical formulation and solution. *J. Atmos. Sci.*, 29:11–37.
- Jaeger, G. S., Lucas, A. J., and Mahadevan, A. (2020a). Formation of interleaving layers in the bay of bengal. *Deep Sea Research Part II: Topical Studies in Oceanography*, 172:104717. Atmosphere-Ocean Dynamics of Bay of Bengal - Volume 2.
- Jaeger, G. S., MacKinnon, J. A., Lucas, A. J., Shroyer, E., Nash, J., Tandon, A., Farrar, J. T., and Mahadevan, A. (2020b). How Spice is Stirred in the Bay of Bengal. *Journal of Physical Oceanography*, 50(9):2669–2688.
- Jiao, W. and Dewar, W. (2015). The energetics of centrifugal instability. *J. Phys. Oceanogr.*, 45:1554–1573.

- 1635 Johnson, L., Lee, C. M., and D'Asaro, E. A. (2016). Global estimates of lateral springtime restratification. *Journal of Physical Oceanography*, 46(5):1555–1573.
- Johnson, L., Lee, C. M., D'Asaro, E. A., Thomas, L., and Shcherbina, A. (2020a). Restratification at a California current upwelling front. part i: Observations. *Journal of Physical Oceanography*, 50(5):1455–1472.
- 1640 Johnson, L., Lee, C. M., D'Asaro, E. A., Wenegrat, J. O., and Thomas, L. N. (2020b). Restratification at a California current upwelling front. part ii: Dynamics. *Journal of Physical Oceanography*, 50(5):1473–1487.
- Johnston, T. S., Schönauf, M. C., Paluszakiewicz, T., MacKinnon, J. A., Arbic, B. K., Colin, P. L., Alford, M. H., Andres, M., Centurioni, L., Gruber, H. C., Helffrich, K. R., Hormann, V., Lemusiaux, P. F., Musgrave, R. C., Powell, B. S., Qiu, B., Rudnick, D. L., Simmons, H. L., Laurent, L. S., Terrill, E. J., Trossman, D. S., Voet, G., Wijesekera, H. W., and Zeiden, K. L. (2019). Flow encountering abrupt topography (float): a multiscale observational and modeling program to understand how topography affects flows in the western North Pacific. *Oceanography*, 32(4):10–21.
- 1645 Khatri, H., Griffies, S. M., Uchida, T., Wang, H., and Menemenlis, D. (2020). A synthesis of upper ocean geostrophic kinetic energy spectra from a global submesoscale permitting simulation. *Earth and Space Science Open Archive*, page 16.
- Klein, P. and Lapeyre, G. (2009). The oceanic vertical pump induced by mesoscale and submesoscale turbulence. *Annu. Rev. Marine Sci.*, 1:351–375.
- 1650 Klein, P., Lapeyre, G., Siegelman, L., Qiu, B., Fu, L.-L., Torres, H., Su, Z., Menemenlis, D., and Le Gentil, S. (2019). Ocean-scale interactions from space. *Earth and Space Science*, 6(5):795–817.
- Klymak, J., Shearman, R., Gula, J., Lee, C., D'Asaro, E., Thomas, L., Harcourt, R., Shcherbina, A., Sundermeyer, M., Molemaker, M., and McWilliams, J. C. (2016). Submesoscale streamers exchange water on the North Wall of the Gulf Stream. *Geophys. Res. Lett.*, 43:1226–1233.
- 1655 Klymak, J. M., Crawford, W., Alford, M. H., MacKinnon, J. A., and Pinkel, R. (2015). Along-isopycnal variability of spicule in the North Pacific. *Journal of Geophysical Research: Oceans*, 120(3):2287–2307.
- Koenig, Z., Fer, I., Kolås, E., Fossum, T. O., Norgren, P., and Ludvigsen, M. (2020). Observations of turbulence at a near-surface temperature front in the Arctic Ocean. *Journal of Geophysical Research: Oceans*, 125(4):e2019JC015526. e2019JC015526 10.1029/2019JC015526.
- Kunze, E., Klymak, J. M., Lien, R.-C., Ferrari, R., Lee, C. M., Sundermeyer, M. A., and Goodman, L. (2015). Submesoscale Water-Mass Spectra in the Sargasso Sea. *Journal of Physical Oceanography*, 45(5):1325–1338.
- 1660 LaCasce, J. H. and Groeskamp, S. (2020). Baroclinic modes over rough bathymetry and the surface deformation radius. *Journal of Physical Oceanography*, pages 1–40.
- Lapeyre, G. (2017). Surface quasi-geostrophy. *Fluids*, 2(1).
- Lapeyre, G. and Klein, P. (2006). Impact of the small-scale elongated filaments on the oceanic vertical pump. *J. Mar. Res.*, 64:1835–851.
- 1665 Lapeyre, G., Klein, P., and Hua, B. L. (2006). Oceanic restratification forced by surface frontogenesis. *Journal of Physical Oceanography*, 36(8):1577–1590.
- Lenn, Y.-D. and Chereskin, T. K. (2009). Observations of Ekman currents in the Southern Ocean. *Journal of Physical Oceanography*, 39(3):768–779.
- Lévy, M., Franks, P. J. S., and Smith, K. S. (2018). The role of submesoscale currents in structuring marine ecosystems. *Nature Communications*, 9(1):4758.
- 1670 Li, C., Zhang, Z., Zhao, W., and Tian, J. (2017). A statistical study on the subthermocline submesoscale eddies in the northwestern Pacific Ocean based on Argo data. *Journal of Geophysical*

- Research: Oceans*, 122(5):3586–3598.
- Lilly, J. M. and Rhines, P. B. (2002). Coherent eddies in the Labrador Sea observed from a mooring. *J. Phys. Oceanogr.*, 32(2):585–598.
- 1685 Lévy, M., Ferrari, R., Franks, P. J. S., Martin, A. P., and Rivière, P. (2012). Bringing physics to life at the submesoscale. *Geophysical Research Letters*, 39(14).
- MacKinnon, J. A., Alford, M. H., Voet, G., Zeiden, K. L., Shaun Johnston, T. M., Siegelman, M., Merrifield, S., and Merrifield, M. (2019). Eddy wake generation from broadband currents near palau. *Journal of Geophysical Research: Oceans*, 124(7):4891–4903.
- 1690 Macvean, M. K. and Woods, J. D. (1980). Redistribution of scalars during upper ocean frontogenesis: A numerical model. *Quarterly Journal of the Royal Meteorological Society*, 106(448):293–311.
- Mahadevan, A. (2016). The impact of submesoscale physics on primary productivity of plankton. *Annual review of marine science*, 8:161–84.
- 1695 Mahadevan, A., D’Asaro, E., Lee, C., and Perry, M. J. (2012). Eddy-driven stratification initiates north atlantic spring phytoplankton blooms. *Science*, 337(6090):54–58.
- Mahadevan, A., Pascual, A., Rudnick, D. L., Ruiz, S., Tintoré, J., and D’Asaro, E. (2020). Coherent Pathways for Vertical Transport from the Surface Ocean to Interior. *Bulletin of the American Meteorological Society*, 101(11):E1996–E2004.
- 1700 Mahadevan, A. and Tandon, A. (2006). An analysis of mechanisms for submesoscale vertical motion at ocean fronts. *Ocean Modelling*, 14:241–256.
- Mahadevan, A., Tandon, A., and Ferrari, R. (2010). Rapid changes in mixed layer stratification driven by submesoscale instabilities and winds. *Journal of Geophysical Research: Oceans*, 115(C3).
- Marshall, J. and Schott, F. (1999). Open-ocean convection: Observations, theory, and models. *Rev. Geophys.*, 37:1–64.
- 1705 McCoy, D., Bianchi, D., and Stewart, A. L. (2020). Global observations of submesoscale coherent vortices in the ocean. *Progress in Oceanography*, 189:102452.
- McDowell, S. and Rossby, H. (1978). Mediterranean water: An intense mesoscale eddy off the bahamas. *Science*, 202:1085–1087.
- 1710 McWilliams, J., Colas, F., and Molemaker, M. (2009). Cold filamentary intensification and oceanic surface convergence lines. *Geophys. Res. Lett.*, 36:L18602.
- McWilliams, J. C. (1984). The emergence of isolated, coherent vortices in turbulent flow. *AIP Conference Proceedings*, 106(1):205–221.
- 1715 McWilliams, J. C. (1985). Submesoscale, coherent vortices in the ocean. *Rev. of Geophys.*, 23:165–182.
- McWilliams, J. C. (2016). Submesoscale currents in the ocean. *Proc. R. Soc. A*, 472(2189).
- McWilliams, J. C. (2017). Submesoscale surface fronts and filaments: secondary circulation, buoyancy flux, and frontogenesis. *Journal of Fluid Mechanics*, 823:391–432.
- 1720 McWilliams, J. C. (2021). Oceanic frontogenesis. *Annual Review of Marine Science*, 13(1):227–253. PMID: 33395349.
- McWilliams, J. C., Gula, J., Molemaker, M., Renault, L., and Shchepetkin, A. (2015). Filament frontogenesis by boundary layer turbulence. *J. Phys. Oceanogr.*, 45:1988–2005.
- 1725 McWilliams, J. C., Gula, J., and Molemaker, M. J. (2019). The gulf stream north wall: Ageostrophic circulation and frontogenesis. *Journal of Physical Oceanography*, 49(4):893–916.
- McWilliams, J. C. and Molemaker, M. (2011). Baroclinic frontal arrest: A sequel to unstable frontogenesis. *J. Phys. Oceanogr.*, 41:601–619.
- 1730 McWilliams, J. C., Molemaker, M., and Yavneh, I. (2001). From stirring to mixing of momentum: cascades from balanced flows to dissipation in the oceanic interior. In *Aha Huliko'a Proceedings*, pages 59–66.
- McWilliams, J. C., Molemaker, M. J., and Yavneh, I. (2004). Ageostrophic, anticyclonic instability

- of a geostrophic, barotropic boundary current. *Physics of fluids*, 16(10):3720–3725.
- Mechoso, C. R. (1980). Baroclinic Instability of Flows Along Sloping Boundaries. *Journal of the Atmospheric Sciences*, 37(6):1393–1399.
- Mensa, J., Garraffo, Z., Griffa, A., Ozgokmen, T., Haza, A., and Veneziani, M. (2013). Seasonality of the submesoscale dynamics in the Gulf Stream region. *Ocean Dynamics*, pages 53–85.
- Molemaker, M., McWilliams, J. C., and Capet, X. (2010). Balanced and unbalanced routes to dissipation in an equilibrated Eady flow. *J. Fluid Mech.*, 654:35–63.
- Molemaker, M., McWilliams, J. C., and Dewar, W. (2015). Submesoscale instability and generation of mesoscale anticyclones near a separation of the California Undercurrent. *J. Phys. Oceanogr.*, 45:613–629.
- Morel, Y., Gula, J., and Ponte, A. (2019). Potential vorticity diagnostics based on balances between volume integral and boundary conditions. *Ocean Modelling*, 138:23 – 35.
- Morrow, R., Fu, L.-L., Arduhin, F., Benkiran, M., Chapron, B., Cosme, E., d’Ovidio, F., Farrar, J. T., Gille, S. T., Lapeyre, G., Le Traon, P.-Y., Pascual, A., Ponte, A., Qiu, B., Raschle, N., Ubelmann, C., Wang, J., and Zaron, E. D. (2019). Global observations of fine-scale ocean surface topography with the surface water and ocean topography (swot) mission. *Frontiers in Marine Science*, 6:232.
- Morvan, M., L’Hégaret, P., Carton, X., Gula, J., Vic, C., Sokolovskiy, M., and Koshel, K. (2019). The life cycle of submesoscale eddies generated by topographic interactions. *Ocean Science Discussions*, 2019:1–20.
- Mukherjee, S., Ramachandran, S., Tandon, A., and Mahadevan, A. (2016). Production and destruction of eddy kinetic energy in forced submesoscale eddy-resolving simulations. *Ocean Modelling*, 105:44 – 59.
- Müller, P., McWilliams, J. C., and Molemaker, M. (2005). Routes to dissipation in the ocean: The 2d/3d turbulence conundrum. In Baumert, H., Simpson, J., and Sundermann, J., editors, *Marine Turbulence: Theories, Observations and Models.*, Cambridge Press.
- Munk, W., Armi, L., Fischer, K., and Zachariasen, F. (2000). Spirals on the sea. *Proceedings of the Royal Society of London. Series A: Mathematical, Physical and Engineering Sciences*, 456(1997):1217–1280.
- Nagai, T., Tandon, A., Yamazaki, H., and Doubell, M. (2009). Evidence of enhanced turbulent dissipation in the frontogenetic Kuroshio Front thermocline. *J. Atmos. Sci.*, 50(14):2159–2179.
- Nagai, T., Tandon, A., Yamazaki, H., Doubell, M. J., and Gallager, S. (2012). Direct observations of microscale turbulence and thermohaline structure in the kuroshio front. *Journal of Geophysical Research: Oceans*, 117(C8).
- Nakamura, N. (1988). Scale selection of baroclinic instability - effects of stratification and non-geostrophy. *J. Atmos. Sci.*, 45(21):3253–3267.
- Napolitano, D. C., da Silveira, I. C. A., Tandon, A., and Calil, P. H. R. (2021). Submesoscale phenomena due to the brazil current crossing of the vitória-trindade ridge. *Journal of Geophysical Research: Oceans*, 126(1):e2020JC016731. e2020JC016731 2020JC016731.
- Naveira Garabato, A. C., Frajka-Williams, E. E., Spingys, C. P., Legg, S., Polzin, K. L., Forryan, A., Abrahamsen, E. P., Buckingham, C. E., Griffies, S. M., McPhail, S. D., Nicholls, K. W., Thomas, L. N., and Meredith, M. P. (2019). Rapid mixing and exchange of deep-ocean waters in an abyssal boundary current. *Proceedings of the National Academy of Sciences*, 116(27):13233–13238.
- Ooyama, K. (1966). On the stability of the baroclinic circular vortex: a sufficient criterion for instability. *Journal of Atmospheric Sciences*, 23(1):43–53.
- Peng, J.-P., Holtermann, P., and Umlauf, L. (2020). Frontal instability and energy dissipation in a submesoscale upwelling filament. *Journal of Physical Oceanography*.
- Perfect, B., Kumar, N., and Riley, J. J. (2018). Vortex structures in the wake of an idealized seamount in rotating, stratified flow. *Geophysical Research Letters*, 45(17):9098–9105.

- Perfect, B., Kumar, N., and Riley, J. J. (2020). Energetics of seamount wakes. part i: Energy exchange. *Journal of Physical Oceanography*, 50(5):1365–1382.
- Pham, H. T. and Sarkar, S. (2018). Ageostrophic secondary circulation at a submesoscale front and the formation of gravity currents. *Journal of Physical Oceanography*, 48(10):2507–2529.
- Poje, A. C., Özgökmen, T. M., Lipphardt, B. L., Haus, B. K., Ryan, E. H., Haza, A. C., Jacobs, G. A., Reniers, A. J. H. M., Olascoaga, M. J., Novelli, G., Griffa, A., Beron-Vera, F. J., Chen, S. S., Coelho, E., Hogan, P. J., Kirwan, A. D., Huntley, H. S., and Mariano, A. J. (2014). Submesoscale dispersion in the vicinity of the deepwater horizon spill. *Proceedings of the National Academy of Sciences*, 111(35):12693–12698.
- Polton, J. A., Lenn, Y.-D., Eliot, S., Chereskin, T. K., and Sprintall, J. (2013). Can drake passage observations match ekman's classic theory? *Journal of physical oceanography*, 43(8):1733–1740.
- Ponte, A., Klein, P., Capet, X., Le Traon, P.-Y., Chapron, B., and Lherminier, P. (2013). Dagnosing surface mixed layer dynamics from high-resolution satellite observations: numerical insights. *J. Phys. Oceanogr.*, 43:1345–1355.
- Price, J. F., Weller, R. A., and Schudlich, R. R. (1987). Wind-driven ocean currents and ekman transport. *Science*, 238(4833):1534–1538.
- Qiu, B., Chen, S., Klein, P., Sasaki, H., and Sasai, Y. (2014). Seasonal mesoscale and submesoscale eddy variability along the north pacific subtropical countercurrent. *Journal of Physical Oceanography*, 44(12):3079 – 3098.
- Ramachandran, S., Tandon, A., Mackinnon, J., Lucas, A. J., Pinkel, R., Waterhouse, A. F., Nash, J., Shroyer, E., Mahadevan, A., Weller, R. A., and Farrar, J. T. (2018). Submesoscale processes at shallow salinity fronts in the bay of bengal: Observations during the winter monsoon. *Journal of Physical Oceanography*, 48(3):479 – 509.
- Rascle, N., Chapron, B., Molemaker, J., Nouguier, F., Ocampo-Torres, F. J., Osuna Cañedo, J. P., Marié, L., Lund, B., and Horstmann, J. (2020). Monitoring intense oceanic fronts using sea surface roughness: Satellite, airplane, and in situ comparison. *Journal of Geophysical Research: Oceans*, 125(8):e2019JC015704. e2019JC015704 10.1029/2019JC015704.
- Rascle, N., Molemaker, J., Marié, L., Nouguier, F., Chapron, B., Lund, B., and Mouche, A. (2017). Intense deformation field at oceanic front inferred from directional sea surface roughness observations. *Geophysical Research Letters*, 44(11):5599–5608.
- Renault, L., McWilliams, J. C., and Gula, J. (2018). Dampening of submesoscale currents by air-sea stress coupling in the californian upwelling system. *Scientific Reports*, 8(1):13388.
- Ruan, X. and Callies, J. (2020). Mixing-driven mean flows and submesoscale eddies over mid-ocean ridge flanks and fracture zone canyons. *Journal of Physical Oceanography*, 50(1):175–195.
- Ruan, X., Thompson, A. F., Flexas, M. M., and Sprintall, J. (2017). Contribution of topographically generated submesoscale turbulence to southern ocean overturning. *Nature Geoscience*, 10:840.
- Rudnick, D. L. and Ferrari, R. (1999). Compensation of horizontal temperature and salinity gradients in the ocean mixed layer. *Science*, 283(5401):526–529.
- Samelson, R. M. and Skillingstad, E. D. (2016). Frontogenesis and turbulence: A numerical simulation. *Journal of the Atmospheric Sciences*, 73(12):5025–5040.
- Sasaki, H., Klein, P., Qiu, B., and Sasa, Y. (2014). Impact of oceanic-scale interactions on the seasonal modulation of ocean dynamics by the atmosphere. *Nature Communications*, 5:5636.
- Sasaki, H., Qiu, B., Klein, P., Sasai, Y., and Nonaka, M. (2020). Interannual to decadal variations of submesoscale motions around the north pacific subtropical countercurrent. *Fluids*, 5(3):116.
- Savelyev, I., Thomas, L. N., Smith, G. B., Wang, Q., Shearman, R. K., Haack, T., Christman, A. J., Blomquist, B., Sletten, M., Miller, W. D., and Fernando, H. J. S. (2018). Aerial observations of symmetric instability at the north wall of the gulf stream. *Geophysical Research Letters*,

- 45(1):236–244.
- Schubert, R., Gula, J., Greatbatch, R. J., Baschek, B., and Biastoch, A. (2020). The Submesoscale Kinetic Energy Cascade: Mesoscale Absorption of Submesoscale Mixed Layer Eddies and Frontal Downscale Fluxes. *Journal of Physical Oceanography*, 50(9):2573–2589.
- 1830 Scott, R. K. (2006). Local and nonlocal advection of a passive scalar. *Phys. Fluids*, 18(116601).
- Shakespeare, C. J. and Taylor, J. R. (2013). A generalized mathematical model of geostrophic adjustment and frontogenesis: uniform potential vorticity. *Journal of Fluid Mechanics*, 736:366–413.
- 1835 Shcherbina, A., D'Asaro, E., Lee, C., Klymak, J., Molemaker, M., and McWilliams, J. (2013). Statistics of vertical vorticity, divergence, and strain in a developed submesoscale turbulence field. *Geophys. Res. Lett.*, 40.
- Shcherbina, A. Y., Gregg, M. C., Alford, M. H., and Harcourt, R. R. (2009). Characterizing Thermohaline Intrusions in the North Pacific Subtropical Frontal Zone. *Journal of Physical Oceanography*, 39(11):2735–2756.
- 1840 Shcherbina, A. Y., Sundermeyer, M. A., Kunze, E., D'Asaro, E., Badin, G., Birch, D., Brunner-Suzuki, A.-M. E. G., Callies, J., Kuebel Cervantes, B. T., Claret, M., Concannon, B., Early, J., Ferrari, R., Goodman, L., Harcourt, R. R., Klymak, J. M., Lee, C. M., Lelong, M.-P., Levine, M. D., Lien, R.-C., Mahadevan, A., McWilliams, J. C., Molemaker, M. J., Mukherjee, S., Nash, J. D., Özgökmen, T., Pierce, S. D., Ramachandran, S., Samelson, R. M., Sanford, T. B., Shearman, R. K., Skillingstad, E. D., Smith, K. S., Tandon, A., Taylor, J. R., Terray, E. A., Thomas, L. N., and Ledwell, J. R. (2015). The latmix summer campaign: Submesoscale stirring in the upper ocean. *Bulletin of the American Meteorological Society*, 96(8):1257–1279.
- Siegelman, L. (2020). Energetic submesoscale dynamics in the ocean interior. *Journal of Physical Oceanography*, 50(3):727–749.
- 1850 Siegelman, L., Klein, P., Rivière, P., Thompson, A. F., Torres, H. S., Flexas, M., and Menemenlis, D. (2020). Enhanced upward heat transport at deep submesoscale ocean fronts. *Nature Geoscience*, 13(1):50–55.
- Skillingstad, E. D. and Samelson, R. M. (2012). Baroclinic frontal instabilities and turbulent mixing in the surface boundary layer. part i: Unforced simulations. *Journal of Physical Oceanography*, 42(10):1701–1716.
- 1855 Skillingstad, E. D. and Samelson, R. M. (2020). Instability processes in simulated finite-width ocean fronts. *Journal of Physical Oceanography*.
- Smith, K. M., Hamlington, P. E., and Fox-Kemper, B. (2016). Effects of submesoscale turbulence on ocean tracers. *Journal of Geophysical Research: Oceans*, 121(1):908–933.
- 1860 Smith, K. S. and Ferrari, R. (2009). The production and dissipation of compensated thermohaline variance by mesoscale stirring. *Journal of Physical Oceanography*, 39(10):2477–2501.
- Solodoch, A., Stewart, A. L., and McWilliams, J. C. (2016). Baroclinic instability of axially symmetric flow over sloping bathymetry. *Journal of Fluid Mechanics*, 799:265–296.
- 1865 Spingys, C. P., Garabato, A. C. N., Legg, S., Polzin, K. L., Abrahamsen, E. P., Buckingham, C. E., Forryan, A., and Frajka-Williams, E. E. (2021). Mixing and transformation in a deep western boundary current: A case study. *Journal of Physical Oceanography*.
- Srinivasan, K., McWilliams, J. C., and Jagannathan, A. (2021). High vertical shear and dissipation in equatorial topographic wakes. *Journal of Physical Oceanography*.
- Srinivasan, K., McWilliams, J. C., Molemaker, M. J., and Barkan, R. (2019). Submesoscale vortical wakes in the lee of topography. *Journal of Physical Oceanography*, 49(7):1949–1971.
- 1870 Srinivasan, K., McWilliams, J. C., Renault, L., Hristova, H. G., Molemaker, J., and Kessler, W. S. (2017). Topographic and mixed layer submesoscale currents in the near-surface southwestern tropical pacific. *Journal of Physical Oceanography*, 47(6):1221 – 1242.
- Stamper, M. A. and Taylor, J. R. (2017). The transition from symmetric to baroclinic instability in

- 1875 the eady model. *Ocean Dynamics*, 67(1):65–80.
- Stegner, A. (2014). *Oceanic Island Wake Flows in the Laboratory*, chapter 14, pages 265–276. American Geophysical Union (AGU).
- Stone, P. (1966). On non-geostrophic baroclinic instability. *J. Atmos. Sci.*, 23:390–400.
- Stone, P. (1970). On non-geostrophic baroclinic instability: Part II. *J. Atmos. Sci.*, 27:721–726.
- 1880 Stone, P. H. (1972). On non-geostrophic baroclinic stability: Part iii. the momentum and heat transports. *Journal of the Atmospheric Sciences*, 29(3):419–426.
- Straneo, F., Kawase, M., and Pickart, R. S. (2002). Effects of wind on convection in strongly and weakly baroclinic flows with application to the labrador sea. *Journal of Physical Oceanography*, 32(9):2603 – 2618.
- 1885 Straub, K. and Kiladis, G. (2002). Observations of a convectively coupled Kelvin wave in the eastern pacific ITCZ. *J. Atmos. Sci.*, 59:30–.
- Su, Z., Torres, H., Klein, P., Thompson, A. F., Siegelman, L., Wang, J., Menemenlis, D., and Hill, C. (2020). High-frequency submesoscale motions enhance the upward vertical heat transport in the global ocean. *Journal of Geophysical Research: Oceans*, 125(9):e2020JC016544. e2020JC016544 2020JC016544.
- 1890 Su, Z., Wang, J., Klein, P., Thompson, A. F., and Menemenlis, D. (2018). Ocean submesoscales as a key component of the global heat budget. *Nat Commun*, 9:775.
- Sullivan, P. P. and McWilliams, J. C. (2018). Frontogenesis and frontal arrest of a dense filament in the oceanic surface boundary layer. *Journal of Fluid Mechanics*, 837:341–380.
- 1895 Sullivan, P. P. and McWilliams, J. C. (2019). Langmuir turbulence and filament frontogenesis in the oceanic surface boundary layer. *Journal of Fluid Mechanics*, 879:512–553.
- Sundermeyer, M. A., Skillingstad, E., Ledwell, J. R., Concannon, B., Terray, E. A., Birch, D., Pierce, S. D., and Cervantes, B. (2014). Observations and numerical simulations of large-eddy circulation in the ocean surface mixed layer. *Geophysical Research Letters*, 41(21):7584–7590.
- 1900 Suzuki, N., Fox-Kemper, B., Hamlington, P. E., and Van Roeke, L. P. (2016). Surface waves affect frontogenesis. *Journal of Geophysical Research: Oceans*, 121(5):3597–3624.
- Tandon, A. and Garrett, C. (1994). Mixed layer restratification due to a horizontal density gradient. *Journal of Physical Oceanography*, 24(6):1419–1424.
- Taylor, J. and Ferrari, R. (2009). The role of secondary shear instabilities in the equilibration of symmetric instability. *J. Fluid Mech.*, 622:103.
- 1905 Taylor, J. R. (2016). Turbulent mixing, restratification, and phytoplankton growth at a submesoscale eddy. *Geophysical Research Letters*, 43(11):5784–5792.
- Taylor, J. R. (2018). Accumulation and subduction of buoyant material at submesoscale fronts. *Journal of Physical Oceanography*, 48(6):1233–1241.
- 1910 Taylor, J. R. and Ferrari, R. (2010). Buoyancy and wind-driven convection at mixed layer density fronts. *Journal of Physical Oceanography*, 40(6):1222–1242.
- Taylor, J. R. and Ferrari, R. (2011). Ocean fronts trigger high latitude phytoplankton blooms. *Geophysical Research Letters*, 38(23).
- Testor, P. and Gascard, J.-C. (2003). Large-scale spreading of deep waters in the western Mediterranean Sea by submesoscale coherent eddies. *J. Phys. Oceanogr.*, 33(1):75–87.
- Thomas, L. (2005). Destruction of potential vorticity by winds. *J. Phys. Oceanogr.*, 35:2457–2466.
- 1915 Thomas, L. and Ferrari, R. (2008). Friction, frontogenesis, and the stratification of the surface mixed layer. *Journal of Physical Oceanography*, 38(11):2501–2518.
- Thomas, L., Tandon, A., and Mahadevan, A. (2008). Submesoscale processes and dynamics. *J. Geophys. Res.*
- 1920 Thomas, L., Taylor, J., Ferrari, R., and Joyce, T. (2013). Symmetric instability in the Gulf Stream. *Deep-Sea Res.*, 91:96–110.

- Thomas, L. N. (2008). Formation of intrathermocline eddies at ocean fronts by wind-driven destruction of potential vorticity. *Dynam. Atmos. Oceans*, 45(3–4):252 – 273.
- 1925 Thomas, L. N. and Taylor, J. R. (2010). Reduction of the usable wind-work on the general circulation by forced symmetric instability. *Geophysical Research Letters*, 37(18):n/a–n/a. L18606.
- Thomas, L. N., Taylor, J. R., D’Asaro, E. A., Lee, C. M., Klymak, J. M., and Shcherbina, A. (2016). Symmetric instability, inertial oscillations, and turbulence at the gulf stream front. *Journal of Physical Oceanography*, 46(1):197–217.
- 1930 Thompson, A. F., Lazar, A., Buckingham, C., Naveira-Garabato, A. C., Damerell, G. M., , and Heywood, K. J. (2016). Open-ocean submesoscale motions: A full seasonal cycle of mixed layer instabilities from gliders. *J. Phys. Oceanogr.*, 46:1285–1307.
- Thompson, L. (2000). Ekman layers and two-dimensional frontogenesis in the upper ocean. *Journal of Geophysical Research: Oceans*, 105(C3):6437–6451.
- 1935 Thorpe, A. and Rotunno, R. (1989). Nonlinear aspects of symmetric instability. *Journal of the atmospheric sciences*, 46(9):1285–1299.
- Torres, H. S., Klein, P., Menemenlis, D., Qiu, B., Su, Z., Wang, J., Chen, S., and Fu, L. (2018). Partitioning ocean motions into balanced motions and internal gravity waves: A modeling study in anticipation of future space missions. *Journal of Geophysical Research: Oceans*.
- 1940 Uchida, T., Balwada, D., Abernathey, R., McKinley, G., Smith, S., and Lévy, M. (2019). The contribution of submesoscale over mesoscale eddy iron transport in the open southern ocean. *Journal of Advances in Modeling Earth Systems*, 11(12):3934–3958.
- Uchida, T., Balwada, D., P. Abernathey, R., A. McKinley, G., K. Smith, S., and Lévy, M. (2020). Vertical eddy iron fluxes support primary production in the open southern ocean. *Nature Communications*, 11(1):1125.
- Vallis, G. K. (2006). *Atmospheric and Oceanic Fluid Dynamics*. Cambridge University Press, Cambridge, U.K.
- van Haren, H. and Millot, C. (2009). Slantwise convection: A candidate for homogenization of deep newly formed dense waters. *Geophysical research letters*, 36(12).
- 1950 Vanneste, J. (1993). The Kelvin-Helmoltz instability in a non-geostrophic baroclinic unstable flow. *Mathl. Comput. Modelling*, 17:149–154.
- Verma, V., Pham, H. T., and Sarkar, S. (2019). The submesoscale, the finescale and their interaction at a mixed layer front. *Ocean Modelling*, 140:101400.
- Vic, C., Gula, J., Roullet, G., and Pradillon, F. (2018). Dispersion of deep-sea hydrothermal vent effluents and larvae by submesoscale and tidal currents. *Deep Sea Res. Pt. I*, 133:1 – 18.
- 1955 Vic, C., Roullet, G., Carton, X., Capet, X., Molemaker, M., and Gula, J. (2015). Eddy-topography interactions and the fate of the Persian Gulf Outflow. *J. Geophys. Res. Oceans*, 120:6700–6717.
- Wang, T., Barkan, R., McWilliams, J. C., and Molemaker, M. J. (2021). Structure of submesoscale fronts of the mississippi river plume. *Journal of Physical Oceanography*.
- 1960 Washington, W. (1964). A note on the adjustment towards geostrophic equilibrium in a simple fluid system. *Tellus*, 16:530–534.
- Wenegrat, J., Thomas, L., Sundermeyer, M., Taylor, J., D’Asaro, E., Klymak, J., Shearman, R., and Lee, C. (2020). Enhanced mixing across the gyre boundary at the gulf stream front. *Proceedings of the National Academy of Sciences*, 0(0):null.
- 1965 Wenegrat, J. O., Callies, J., and Thomas, L. N. (2018a). Submesoscale baroclinic instability in the bottom boundary layer. *Journal of Physical Oceanography*, 48(11):2571–2592.
- Wenegrat, J. O. and McPhaden, M. J. (2016). Wind, waves, and fronts: Frictional effects in a generalized ekman model. *Journal of Physical Oceanography*, 46(2):371–394.
- 1970 Wenegrat, J. O. and Thomas, L. N. (2020). Centrifugal and symmetric instability during ekman adjustment of the bottom boundary layer. *Journal of Physical Oceanography*, 0(0):null.

- Wenegrat, J. O., Thomas, L. N., Gula, J., and McWilliams, J. C. (2018b). Effects of the submesoscale on the potential vorticity budget of ocean mode waters. *Journal of Physical Oceanography*, 48(9):2141–2165.
- 1975 Whitt, D. B., Lévy, M., and Taylor, J. R. (2019). Submesoscales enhance storm-driven vertical mixing of nutrients: Insights from a biogeochemical large eddy simulation. *Journal of Geophysical Research: Oceans*, 124(11):8140–8165.
- Whitt, D. B. and Taylor, J. R. (2017). Energetic submesoscales maintain strong mixed layer stratification during an autumn storm. *Journal of Physical Oceanography*, 47(10):2419–2427.
- 1980 Wijesekera, H. W., Shroyer, E., Tandon, A., Ravichandran, M., Sengupta, D., Jinadasa, S., Fernando, H. J., Agrawal, N., Arulananthan, K., Bhat, G., et al. (2016). Asiri: An ocean–atmosphere initiative for bay of bengal. *Bulletin of the American Meteorological Society*, 97(10):1859–1884.
- Yang, Y., McWilliams, J. C., Liang, X. S., Zhang, H., Weisberg, R. H., Liu, Y., and Menemenlis, D. (2021). Spatial and temporal characteristics of the submesoscale energetics in the gulf of mexico. *Journal of Physical Oceanography*, 51(2):475 – 489.
- 1985 Yankovsky, E. and Legg, S. (2018). Symmetric and Baroclinic Instability in Dense Shelf Overflows. *Journal of Physical Oceanography*, 49(1):39–61.
- Young, W. (1994). The subinertial mixed layer approximation. *Journal of physical oceanography*, 24(8):1812–1826.
- 1990 Young, W. a. and Jones, S. (1991). Shear dispersion. *Physics of Fluids A: Fluid Dynamics*, 3(5):1087–1101.
- Yu, X., Garabato, A. C. N., Martin, A. P., and Marshall, D. P. (01 Dec. 2020). The annual cycle of upper-ocean potential vorticity and its relationship to submesoscale instabilities. *Journal of Physical Oceanography*.
- 1995 Yu, X., Naveira Garabato, A. C., Martin, A. P., Buckingham, C. E., Brannigan, L., and Su, Z. (2019a). An annual cycle of submesoscale vertical flow and restratification in the upper ocean. *Journal of Physical Oceanography*, 49(6):1439–1461.
- Yu, X., Naveira Garabato, A. C., Martin, A. P., Gwyn Evans, D., and Su, Z. (2019b). Wind-forced symmetric instability at a transient mid-ocean front. *Geophysical Research Letters*, 46(20):11281–11291.
- 2000 Zhang, Z., Zhang, X., Qiu, B., Zhao, W., Zhou, C., Huang, X., and Tian, J. (2020). Submesoscale currents in the subtropical upper ocean observed by long-term high-resolution mooring arrays. *Journal of Physical Oceanography*, pages 1–65.